

A chemical bonding based descriptor for predicting the impact of quantum nuclear and anharmonic effects on hydrogen-based superconductors

Francesco Belli,[†] Eva Zurek,^{*,†} and Ion Errea^{*,‡,¶,§}

[†]*Department of Chemistry, State University of New York at Buffalo, Buffalo, NY 14260-3000, USA*

[‡]*Fisika Aplikatua Saila, Gipuzkoako Ingeniaritza Eskola, University of the Basque Country (UPV/EHU), Europa Plaza 1, 20018 Donostia/San Sebastián, Spain*

[¶]*Centro de Física de Materiales (CFM-MPC), CSIC-UPV/EHU, Manuel de Lardizabal Pasealekua 5, 20018 Donostia/San Sebastián, Spain*

[§]*Donostia International Physics Center (DIPC), Manuel de Lardizabal Pasealekua 4, 20018 Donostia/San Sebastián, Spain*

E-mail: ezurek@buffalo.edu; ion.errea@ehu.eus

Abstract

Quantum nuclear effects (QNEs) can significantly alter a material's crystal structure and phonon spectra, impacting properties such as thermal conductivity and superconductivity. However, predicting *a priori* whether these effects will enhance or suppress superconductivity, or destabilize a structure, remains a grand challenge. Herein, we address this unresolved problem by introducing a descriptor, based upon the integrated crystal orbital bonding index (iCOBI), to predict the influence of QNEs on a crystal lattice's dynamic stability, phonon spectra and superconducting properties. We find that structures with atoms in symmetric chemical bonding environments exhibit greater resilience to structural perturbations induced by QNEs, while those with atoms in asymmetric bonding environments are more susceptible to structural alterations, resulting in enhanced superconducting critical temperatures.

Introduction

Achieving room-temperature and room-pressure superconductivity would benefit society in unforeseeable ways. Hydrogen-rich systems are the most promising compounds that could achieve this feat, as their strong electron phonon coupling (EPC) and large Debye temperatures allow them, in principle, to possess high superconducting critical temperatures, T_c s, as originally proposed by Ashcroft^{1,2}. Additionally, since the pairing mechanism in hydrides is presumed to be conventional, their superconducting properties can often be reasonably well predicted by theory, opening the door towards rational materials design. Indeed, many hydrides with high T_c s have been synthesized, though at pressures impractical for applications. This includes H_3S ($T_c = 203$ K near 150 GPa)³, LaH_{10} ($T_c = 250$ -260 K near 200 GPa^{4,5}), YH_4 ($T_c = \sim 88$ K at 155 GPa⁶), YH_6 ($T_c = 220$ K at 160-180 GPa^{7,8}), YH_9 ($T_c = 240$ K at 200 GPa⁸), CaH_6 ($T_c = 210$ -215 K at 160-172 GPa^{9,10}), $(La,Y)H_6$ and $(La,Y)H_{10}$ ($T_c = 237$ and 253 K, respectively, both between 170-196 GPa¹¹), as well as $LaBeH_8$ ($T_c = 110$ K at 80 GPa¹²), $(La,Ce)H_{9-10}$ ($T_c = 176$ K at 100 GPa¹³) and $Y_{0.5}Ce_{0.5}H_9$ ($T_c = 97$ -141 K between 98-200 GPa¹⁴), to name a few.

As alluded to above, first-principles calculations based on density functional theory (DFT) have proven to be a valuable tool to direct experimental results¹⁵⁻¹⁷, and many of the experimental discoveries have been anticipated by DFT calculations¹⁸⁻²². Furthermore, through DFT-based crystal structure prediction (CSP) methods, the landscape of hydrogen-host binary combinations has been meticulously explored. As a result, a clear understanding of the features enhancing superconductivity in electron-phonon mediated hydrogen-based superconductors has emerged^{15,23,24}. Compounds with weakened covalent bonds, elevated hydrogen content, symmetric bonding configurations, and a high density of states (DOS) at the Fermi level (E_F), with a large contribution arising from the hydrogen atoms, are likely to exhibit a high T_c . Such insights are now being applied to direct the *ab initio* exploration of the phase diagrams of ternary and quaternary hydrides²⁵⁻³¹. The hope is to further expand the list of predicted compounds (including those that are metastable), and scout for low-pressure-synthesizable systems, which would be necessary for practical applications of

hydrogen-based superconductors.

The typical workflow³² for the *ab initio* prediction of hydrogen-based superconductors begins with identifying promising structures that correspond to (low energy) local or global minima in the Born-Oppenheimer energy surface (BOES). Next, the dynamic stability of the predicted compounds is determined by calculating the vibrational phonon frequencies in the harmonic approximation, and ensuring that no imaginary eigenvalues are present. This corresponds to a classic treatment of the nuclei, which are assumed to vibrate around their local minima. If, instead, the nuclei are treated as quantum particles, their positions are not clamped, but fluctuate around an average atomic position, known as a centroid. In this case, the phonon frequencies should be calculated from the second derivative of the total free energy with respect to the centroid positions, which includes the kinetic energy associated to the ionic quantum fluctuations. In hydrogen rich compounds, the harmonic classical treatment of the nuclei can yield predictions that differ vastly from those obtained with a proper quantum anharmonic treatment of the ions due to the light mass of hydrogen and the dynamical instabilities predicted at the harmonic level because of their potentially very large EPC³³. The properties that are affected by quantum nuclear effects (QNEs) and anharmonicity in hydrides include: the optimized geometries, phonon frequencies, and perhaps most significantly for the current study, the superconducting behavior. These effects were shown to be extremely important for the first two high pressure hydrides that were synthesized, LaH₁₀³³ and H₃S³⁴. For example, DFT-based CSP searches found an $Fm\bar{3}m$ symmetry LaH₁₀ structure to be the most stable at high pressures, but below 230 GPa other distorted variants were preferred, suggesting a complex BOES with many local minima.^{21,22,33,35} However, within the harmonic approximation none of the proposed LaH₁₀ phases (including $Fm\bar{3}m$) are dynamically stable below 230 GPa, so their T_c cannot be calculated. At the same time, experiments measured a T_c of 250 K from 137-218 GPa³ or 260 K at 188 GPa⁴ for a presumed LaH₁₀ stoichiometry compound, resulting in a discrepancy between theory and experiment. This discrepancy could only be solved when QNEs were taken into account³³. Since then, it has been shown that QNEs have a profound impact on the stability and superconducting properties of numerous high³⁶⁻³⁸ and ambient-pressure^{39,40} hydrides.

Though a number of computational techniques have been developed for treating QNEs and anharmonicity, the method that is often applied to superconducting hydrides is the stochastic self-consistent harmonic approximation (SSCHA)^{41–45}. Recently, workflows that accelerate SSCHA calculations by leveraging machine-learned interatomic potentials have been developed^{40,46,47}. Therefore, we can expect the number of SSCHA-based studies on hydrides to grow. However, the general trends of how QNEs and anharmonicity impact the superconducting properties of hydrogen-rich compounds is still not clear. In some cases they largely suppress superconductivity – a prime example being PdH where the strong anharmonicity of the material leads to an overestimation of the T_c by almost a factor of four (~ 35 K harmonic vs. ~ 10 K experiment)^{39,41}, while in other situations, T_c can be considerably increased, such as in LaBH₈, where QNEs enhance the T_c from about 100 K to 160 K at 100 GPa⁴⁸.

Herein, by collecting a series of systems where QNEs and anharmonicity were treated through the SSCHA, we show the emergence of two possible scenarios. In the first, when inclusion of quantum nuclear effects does not perturb the geometry of a structure, they lower the T_c . Conversely, when quantum treatment of the lattice changes its geometrical parameters, a concomitant increase in T_c is observed. Furthermore, we develop a chemical bonding based descriptor that can predict which of these two scenarios describe a particular hydride. This descriptor, based upon a vector sum of the integrated crystal orbital bonding index (iCOBI)⁴⁹, is facile to compute, thereby enabling the automated classification of any arbitrary hydride into one of the two possible types. Our study results in a comprehensive, chemical bonding inspired understanding of the impact of QNEs and anharmonicity on the structures and phonon modes of hydrogen-based compounds, offering the possibility of discerning in advance their impact on the superconducting properties.

Methods

The structural parameters and Eliashberg spectral functions, both with and without SSCHA-treated QNEs, were obtained from the literature. The dataset includes the following compounds: PdH at

ambient pressure³⁹, AlH₃ at 135 GPa³⁶, LaH₁₀ at 250 GPa⁵⁰, a phase of atomic hydrogen ($I4_1/amd$ at 500 GPa⁵¹), PtH at 100 GPa⁴¹, YH₆ at 150 GPa⁷, H₃S- $Im\bar{3}m$ at 250 GPa and 130 GPa³⁴, ScH₆- $P6_3/mmc$ at 140 GPa³⁷, ScH₆- $Cmcm$ at 100 GPa, H₃S- $R3m$ at 130 GPa³⁴, LaBH₈ at 100 GPa⁴⁸, and a phase of molecular hydrogen ($Cmca-4$ at 450 GPa⁵²). Moreover, additional calculations were performed to obtain data for ScH₆- $Cmcm$ at 100 GPa, as described below. All these listed spacegroups and pressures correspond to the classical calculation, excluding the potential impact on the structure and the estimated pressure of NQEs.

In most of these investigations^{7,34,36,37,41,48,50-52}, the geometries were initially optimized within the Born-Oppenheimer approximation at the specified pressures. The SSCHA was subsequently applied to relax the atomic positions including NQEs and anharmonicity, while keeping the unit cell shape and dimensions fixed. This approach allows for a direct comparison of the phonons and the Eliashberg spectral functions at identical volumes; however, the pressures determined via SSCHA are higher from those computed using classical nuclei due to the extra contribution arising from the QNEs. In contrast, the comparative analysis between the classical and quantum structures for ScH₆- $Cmcm$ at 100 GPa and ScH₆- $P6_3/mmc$ at 140 GPa was conducted by relaxing the structures with the SSCHA also at 100 and 140 GPa, respectively, which implies that the lattices in the comparison are different in these two cases.

The ScH₆- $Cmcm$ phase was identified by displacing the atoms according to the eigenvectors of the imaginary E_{2g} symmetry mode at Γ computed for ScH₆- $P6_3/mmc$ at 100 GPa³⁷, followed by a subsequent structural relaxation. The DFT calculations for ScH₆- $Cmcm$ were performed with the plane-wave Quantum ESPRESSO package^{53,54}. We employed the Perdew-Burke-Ernzerhof⁵⁵ parameterization of the exchange-correlation potential (PBE-GGA), along with ultrasoft pseudo-potentials that treated 11 electrons of scandium in the valence, with cutoffs for the wavefunctions and density chosen as 1088 eV and 10,884 eV, respectively. The Brillouin zone integration in the self-consistent calculations were performed with a first-order Methfessel-Paxton smearing with a broadening of 0.27 eV, and a k-mesh with a spacing of $2\pi \times 0.011 \text{ \AA}^{-1}$. The harmonic phonon calculations were performed on a q-mesh with a spacing of $2\pi \times 0.056 \text{ \AA}^{-1}$, making use of density

functional perturbation theory⁵⁶. The electron-phonon interaction was calculated on a k-mesh with a spacing of $2\pi \times 0.0083 \text{ \AA}^{-1}$, with a Gaussian smearing of 0.11 eV to approximate the Dirac deltas, and with the same phonon grid that was used in the phonon calculations. The T_c for all compounds were recalculated using the isotropic Migdal-Eliashberg⁵⁷ formalism with a Coulomb repulsion parameter, μ^* , of 0.1.

To analyze the bonding, DFT calculations for all of the structures in our dataset were performed using the Vienna *ab initio* Simulation Package (VASP)⁵⁸, with the PBE-GGA and an energy cut-off of 800 eV. The number of valence electrons treated explicitly and their electronic configurations are reported in Table S1. The core electrons were treated with the projector augmented wave (PAW) method⁵⁹. The reciprocal space was sampled using a Γ -centered Monkhorst-Pack⁶⁰ k-mesh with a spacing of $2\pi \times 0.016 \text{ \AA}^{-1}$ with an electronic smearing of 0.2 eV. The integrated Crystal Orbital Bonding Index (iCOBI)⁴⁹, which is a quantification of the extent of covalent bond formation, was calculated for atom pairs using the LOBSTER⁶¹ code with the standard basis set proposed.

Results and Discussion

Two classes of structures

We begin by introducing the compounds that will be considered in our foray into the impact of QNEs on the properties of superconducting hydrides. Their structures and computed superconducting parameters have been taken from the cited literature, with the exception of the calculations outlined in the *Methods* section. As we will soon see, each one has its own story of how it is impacted by QNEs. As might be surmised by the reader, the way in which QNEs manifest themselves for the “Type I” systems described below differs markedly from how it influences compounds that belong to the “Type II” class.

Figure 1 illustrates the Type I crystal lattices and provides the pressure at which they have been computationally investigated. It turns out that the high symmetry of these lattices, and absence

of free parameters in their Wyckoff positions, is key in determining the way in which they are impacted by QNEs. The first system to be described is PdH, which assumes a face-centered-cubic ($Fm\bar{3}m$) structure at ambient pressure ($1 \text{ atm} = 1.01325 \times 10^4 \text{ Pa}$, in our calculations). A hallmark of conventional, or electron-phonon mediated, superconductors is that their T_c decreases upon substitution of a lighter isotope by a heavier one, because lighter atoms experience higher frequency vibrations. In a conventional superconductor with one type of atom of mass M , it is expected that $T_c \propto M^{-\alpha}$, where $\alpha = 0.5$ is the isotope coefficient. However, in PdH this coefficient is negative – a consequence of QNEs³⁹ – such that its measured T_c is $\sim 20\%$ lower than that of its heavier brethren, PdD^{62–68}. The next phase that we considered, AlH_3 - $Pm\bar{3}n$, is one of the first high-pressure hydrides to be theoretically⁶⁹ and experimentally⁷⁰ studied. Though calculations assuming classic nuclei predicted superconductivity, none could be measured down to 4 K⁷⁰, and this discrepancy was shown to be a consequence of QNEs^{36,71}. As already alluded to above, without the inclusion of QNEs LaH_{10} - $Fm\bar{3}m$ is predicted to be dynamically unstable⁵⁰ in a pressure range where it was synthesized and its superb superconducting properties were measured^{4,5}, becoming dynamically stable with classical nuclei only above $\sim 230 \text{ GPa}$. A hypothetical high-pressure phase of atomic hydrogen with $I4_1/amd$ symmetry computed to be the ground state above 577 GPa in the presence of QNEs with a T_c approaching 800 K at 2 TPa^{72–75} was also considered. As was a likely candidate of a synthesized hydride of platinum⁷⁶ (PtH - $P6_3/mmc$), which was calculated to have a T_c of 12 K at 90 GPa^{76–78}, but whose superconductivity was shown to be suppressed upon the inclusion of QNEs⁴¹. In synthesized YH_6 - $Im\bar{3}m$ the measured T_c (224 K at 166 GPa⁷) is lower than predictions that do not treat the nuclei quantum mechanically (264 K at 120 GPa⁷⁹). Turning to the experimentally synthesized H_3S phase³, we consider in this class the $Im\bar{3}m$ structure, which is predicted to become enthalpically preferred over the $R\bar{3}m$ symmetry phase above 175 GPa^{18,34} when treating ions classically, but QNEs extend its range of dynamic stability down to $\sim 100 \text{ GPa}$ (though it may not be the thermodynamic minimum at this pressure). All these structures in this Type I class show a high symmetry in their bonding environment.

The Type II family (Figure 2) includes two predicted ScH_6 phases with H_2 molecular units,

Type I structures: high symmetry in bonding

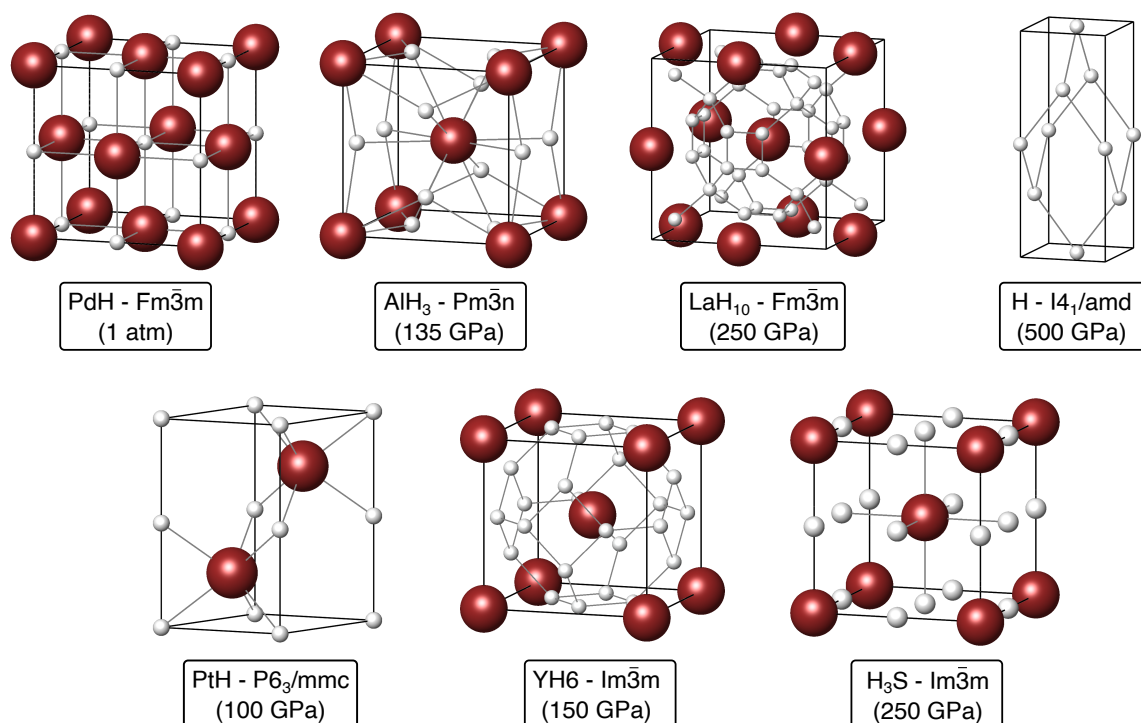


Figure 1: Crystal structures of the Type I class of compounds. Locally, these phases exhibit a high degree of symmetry in their bonding environments. Hydrogen atoms are white, and all other atom types are colored reddish-brown.

which were thermodynamically preferred over the $Im\bar{3}m$ ScH_6 clathrate structure below 275 GPa⁸⁰. Diatomic hydrogen motifs comprise the hydrogenic sublattice in both, with the main difference between them being that the bond distances within the H_2 molecules in the higher pressure phase ($P6_3/mmc$) are the same, while in the lower pressure phase ($Cmcm$) they differ. Moreover, a distorted H_3S structure, of $R\bar{3}m$ symmetry, which DFT calculations predict to be enthalpically preferred over $Im\bar{3}m$ H_3S below 175 GPa was considered^{81,82}. In the rhombohedral distortion three H-S distances become shorter than the others, thereby breaking the octahedral symmetry about the sulfur atoms that is present in the cubic phase. This distortion is associated with a large measured drop in T_c , which was experimentally observed at 150 GPa signifying a small discrepancy between the predicted and measured pressure of the phase transition.^{3,83,84} We also examined $LaBH_8$, the first ternary hydride proposed that can be derived from LaH_{10} by removing the hydrogen atoms from the $8c$ Wyckoff position, and adding boron atoms to the $4a$ position.^{29,31,85} A number of

Type II structures: reduced symmetry in bonding

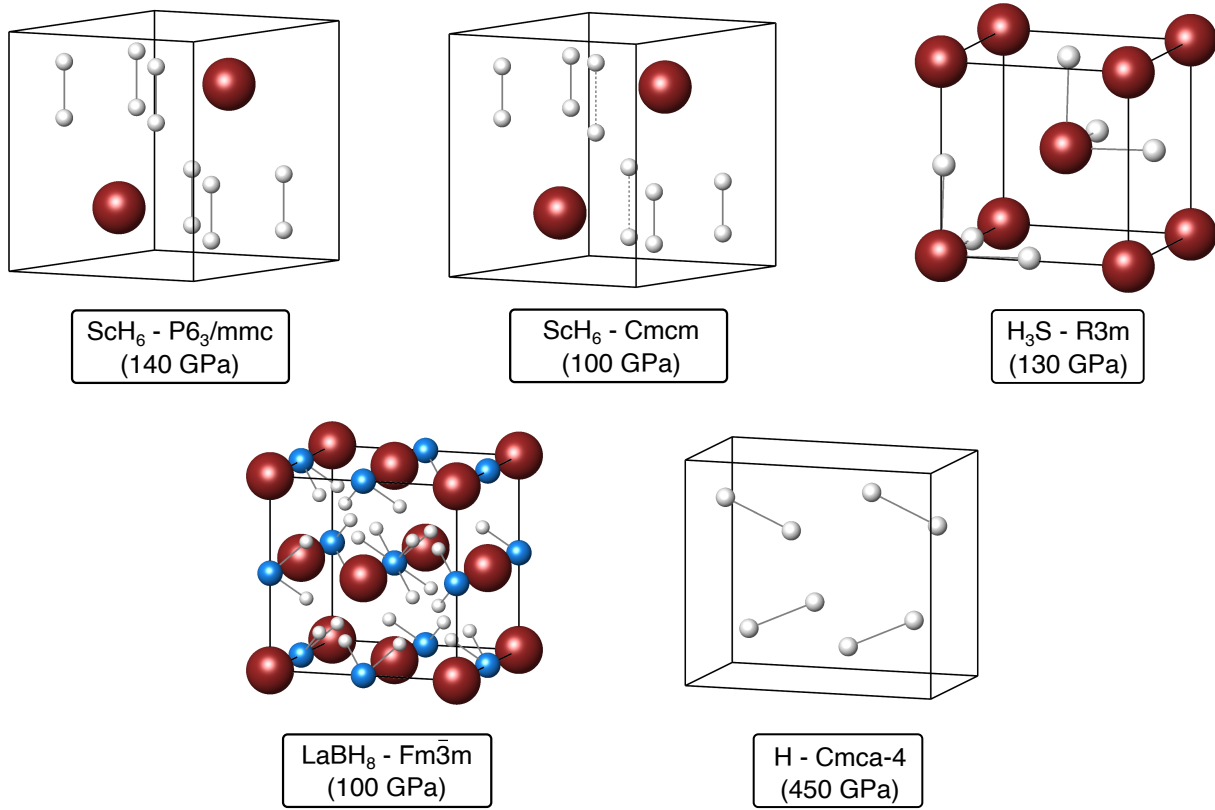


Figure 2: Crystal structures of the Type II class of compounds. Locally, these phases exhibit a lower degree of symmetry in their bonding environments than the Type I compounds (Figure 1). Hydrogen atoms are white, B atoms in LaBH_8 are blue, and all other atom types are colored reddish-brown. The $\text{H}-Cmca-4$ notation corresponds to the primitive cell, while here the conventional cell is shown.

compounds with this structure type, but varying the identity of the electropositive and p -block elements, have been predicted,^{85,86} and superconductivity has been measured in isotypic LaBeH_8 .¹² Finally, we considered the $Cmca-4$ phase of hydrogen⁸⁷, composed of layered pairs of molecular hydrogen units in an ABAB hexagonal close packed stacking, which was predicted via static lattice calculations to be the most stable structure between 350-450 GPa⁸⁸, or at 220 GPa and 300 K⁸⁹, with a T_c of 242 K at 450 GPa⁹⁰. More recent investigations, accounting for QNEs, have proposed a refined phase diagram where a $Cmca-12$ phase is the most stable between 410-577 GPa, while also suggesting that $Cmca-4$ is not the ground state at any pressure.⁷³ The local bonding in all these Type II structures is less symmetric than those in the Type I class.

Quantum nuclear effects on the structural and superconducting properties

Now that we have described the structural characteristics of the considered compounds, let us examine the properties that are related to their superconducting response. The key quantity for calculating the T_c in conventional superconductors is the Eliashberg spectral function, $\alpha^2 F(\omega)$, which can be understood as a phonon density of states, $F(\omega)$, weighted by the energy-dependent electron-phonon coupling, $\alpha(\omega)$. Though $\alpha^2 F(\omega)$ can, in principle, be measured (*e.g.* via inelastic tunneling spectroscopy⁹¹), it may be easier to calculate it via one of the various first-principles techniques that are available. Figure 3 plots the variation of $\alpha^2 F(\omega)$ as a function of frequency computed with classical nuclei and neglecting anharmonicity (grey), as compared to a SSCHA calculation incorporating quantum anharmonic effects on the structure and the phonons at zero temperature (red). It is not uncommon for QNEs to expand the volume by a value that corresponds to ~ 10 GPa³³, but for clarity here the two calculations are performed at the same volume. This comparison allows us to estimate, at the same time, the impact of QNEs and anharmonicity on the phonon spectra and the electron-phonon matrix elements. If we were to compare the $\alpha^2 F(\omega)$ functions computed at the same pressure, it would not be possible to conclude if the difference between them was a result of the different volumes, or because of QNEs.

Due to their high symmetry and absence of free parameters in the Wyckoff positions, relaxation incorporating QNEs does not affect the structural coordinates of most of the Type I compounds illustrated in Figure 1 (PdH- $Fm\bar{3}m$, AlH₃- $Pm\bar{3}n$, H- $I4_1/amd$, PtH- $P6_3/mmc$, YH₆- $Im\bar{3}m$, and H₃S- $Im\bar{3}m$). Because LaH₁₀- $Fm\bar{3}m$ has a single free parameter, which is related to the 32f Wyckoff site occupied by a hydrogen atom, QNEs can, in principle, alter this atomic position. However, after SSCHA relaxation we observed that the variation in this coordinate is negligible, consistent with the other phases belonging to this class of hydrides.

Comparison of the red and grey $\alpha^2 F(\omega)$ curves in the top panel of Figure 3 reveals that QNEs tend to induce a blue shift of the phonon spectra in Type I compounds, and this effect is most pronounced for the lower optical branches. Because these modes contribute significantly to the

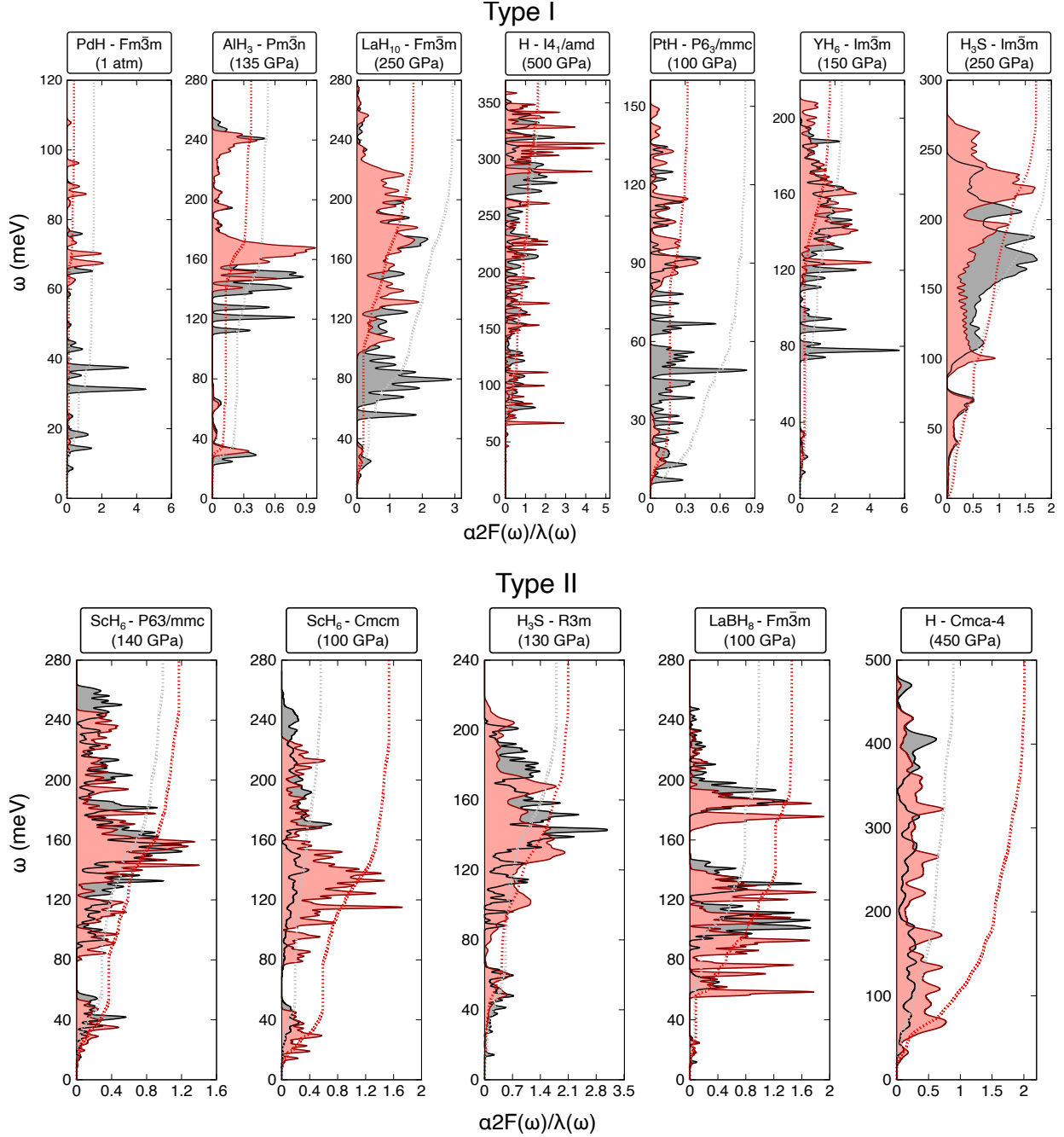


Figure 3: The Eliashberg spectral function (shaded curve, $\alpha^2F(\omega)$), along with the integrated electron-phonon-coupling parameter (dashed line, $\lambda(\omega)$), for the Type I (upper panel) and Type II (lower panel) structures illustrated in Figure 1 and Figure 2, respectively. Results for classical (quantum) nuclei are given in grey (red).

EPC constant, and $\lambda \propto \omega^{-2}$, this phonon hardening tends to suppress λ (Figure S2), and also T_c . At the pressures considered T_c decreases from 47 K to 5 K for PdH, 13.7 K to 3 K for AlH₃, 260 K to 220 K for LaH₁₀, 14.5 K to 0.4 K for PtH, 272 K to 247 K for YH₆, and from 226 K to 190 K

for H_3S (Table S3). The only exception to this trend is $\text{H-}I4_1/amd$, where QNEs produce a red shift of the acoustic phonon branches, but a blue shift of the optical phonon branches, resulting in a nearly negligible effect on both λ and T_c (320 K versus 300 K), although when the volume expansion induced by QNEs is considered, the impact is a bit larger.⁹²

Let us now pivot now to the Type II structures shown in Figure 2, whose Eliashberg spectral functions are illustrated in the bottom panel of Figure 3. Both of the ScH_6 phases considered contain dihydrogen molecules that interact weakly with one another, and more strongly with scandium via charge transfer from the electropositive element to the hydrogen, coupled with $\text{H}_2 \sigma \rightarrow \text{Sc } d$ donation and $\text{Sc } d \rightarrow \text{H}_2 \sigma^*$ back-donation.⁹³⁻⁹⁵ These metal- H_2 interactions result in an elongation of the dihydrogen bond relative to what it would be in the molecular phase at the given pressure.⁹⁵ In $\text{ScH}_6\text{-}P6_3/mmc$ at 140 GPa QNEs lengthen this bond even further, from 1.02 to 1.08 Å, with a concomitant red shift of the phonon modes and an increase in T_c from 88 K to 99 K. When the nuclei are treated classically, the ground state of ScH_6 assumes $Cmcm$ symmetry at 100 GPa. This phase can be derived from the higher-pressure $P6_3/mmc$ structure by breaking the symmetry and decreasing the distance between two sets of hydrogen atoms to 0.95 Å, and increasing the distance between another pair of H atoms to 1.28 Å. Therefore, the classical $\text{ScH}_6\text{-}Cmcm$ lattice can be better described as $[\text{Sc}^{2+}][2\text{H}^-]\cdot 2\text{H}_2$. However, quantum lattice fluctuations restore the broken symmetry, so all of the H-Sc bonds optimize to 1.08 Å at 100 GPa within the SSCHA, resulting in a 5-fold increase in the T_c from 20 K to 108 K.

A similar phenomenon occurs in $\text{H}_3\text{S-}R3m$, which experiments suggest is preferred over the higher symmetry $Im\bar{3}m$ structure below 150 GPa⁸³. At a volume corresponding to a classical pressure of 130 GPa, QNEs increase the pressure to ~ 140 GPa. Moreover, they symmetrize the H-S bonds, which range from 1.46-1.66 Å in the classic lattice, such that they all optimize to 1.56 Å in the quantum lattice. The change in these bond lengths shifts the Eliashberg spectral function to lower frequencies, with a concomitant increase in the T_c from 175 K to 214 K. Though, in principle, a similar result would be expected for LaH_{10} (at a pressure low enough so that the $Fm\bar{3}m$ phase is no longer the classical ground state⁵⁰), we were unable to obtain a distorted lower-symmetry

structure with a small enough unit cell to permit an *ab initio* calculation of the electron-phonon interaction.

Because LaBH_8 - $Fm\bar{3}m$ can be derived from LaH_{10} , its structure also possesses a free parameter for the hydrogen atoms situated at the 32f Wyckoff positions. Within LaBH_8 this parameter determines the B-H distance. Whereas in LaH_{10} - $Fm\bar{3}m$ the inclusion of QNEs does not have a notable impact on the positions of these hydrogen atoms, the behavior is different within LaBH_8 - $Fm\bar{3}m$. Specifically, QNEs elongate and weaken the B-H bond from 1.366 to 1.385 Å, with a concomitant softening of the frequency associated with its vibration. As a result, the phonon spectra undergo a red shift and the T_c increases from 97 K to 143 K at 100 GPa. Additionally, QNEs tend to destabilize this structure due to the stretching of the B-H bond, rendering it unstable at 77 GPa, a much higher pressure than the 35 GPa expected for classic nuclei^{30,48}. This behavior is opposite to what has been found for H_3S ⁵⁰ and LaH_{10} ,³⁴ where the pressure domain of dynamic stability is increased by QNEs. Finally, in the last Type II structure considered, a molecular H_2 phase with $Cmca$ symmetry and four hydrogen atoms in the primitive cell, QNEs elongate the H-H distances from 0.78 to 0.83 Å at 400 GPa, weakening this bond with a concomitant red shift of the phonon modes, and a remarkable increase in the T_c from 109 K to 258 K.

A descriptor for the impact of quantum nuclear effects on T_c

As described in the previous section, QNEs impact the geometries and structural features of the hydrogen-rich systems considered herein. Both these geometrical perturbations and anharmonicity can modify the frequencies associated with the phonon modes, which in turn affect the T_c . Because symmetry lowering (*e.g.* Jahn-Teller or Peierls) distortions typically lead to the opening of gaps or pseudogaps, whereas symmetry raising transformations tend to increase the number of states that can participate in the EPC mechanism, QNE-induced structural changes could also vary the DOS at E_F , with a concomitant effect on the electron-phonon matrix elements and therefore on the resulting T_c . For the systems studied here belonging to Type I, the practical absence of structural changes

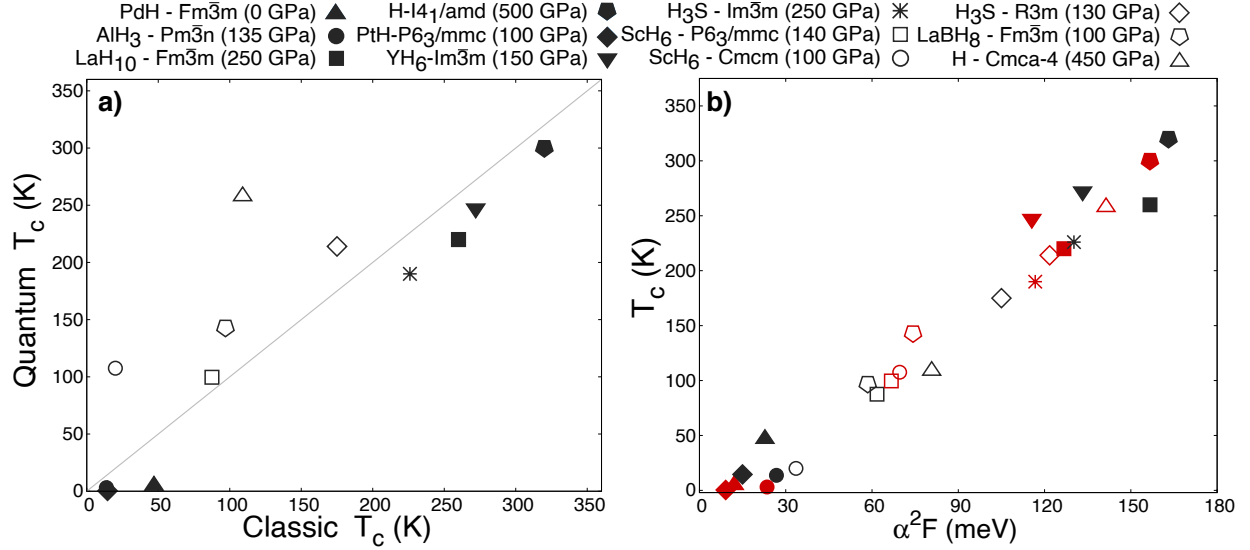


Figure 4: (a) The superconducting critical temperature, T_c , computed for quantum nuclei versus classic nuclei for the Type 1 (Figure 1) and Type 2 (Figure 2) compounds studied herein. The open symbols (Type II) fall above the diagonal line and represent those compounds whose quantum T_c s are larger than their classic T_c s, while the quantum T_c s of the compounds denoted by the dark symbols (Type I) are lower than their classical T_c s. (b) The classical (black) and quantum (red) T_c s of the studied compounds as a function of the Eliashberg spectral function, $\alpha^2 F(\omega)$. The legend above the plots provides the symbol associated with each compound.

makes the DOS at E_F insensitive to NQEs, therefore any variations in T_c were mostly a result of the changes in the phonon frequencies. The systems in Type II class, however, undergo structural changes that in general tend to increase the DOS at the Fermi level, making the electron-phonon coupling larger. This is evident for H-*Cmca-4* and ScH₆-*Cmcm*, where the increased number of states at the Fermi level due to NQEs makes the value of the Eliashberg function much larger than in the classical nuclei case. Accordingly, in these cases the impact of NQEs is not only a shift of the phonon frequencies, but a more complex scenario in which the Fermi surface changes increase the coupling between the electrons and the ionic lattice. As highlighted by Figure 4(a), NQEs typically decrease the T_c in Type I compounds, whereas for the Type II systems they tend to increase it, at times by a staggering factor of two (H-*Cmca-4*) or even four (ScH₆-*Cmcm*) when their impact on the Fermi surface is remarkable.

Interestingly, we have found that the integral of the Eliashberg spectral function, defined as $\alpha^2 F = \int_0^\infty \alpha^2 F(\omega) d\omega$, correlates very well with the T_c obtained for both classic harmonic and

quantum anharmonic calculations (Figure 4(b)). This finding indicates that $\alpha^2 F$ itself is a robust descriptor for analysing how QNEs impact T_c . In fact, it correlates much better than the electron-phonon coupling constant, λ , and the average of the logarithmic phonon frequency, ω_{\log} , the prefactor in the Allen-Dynes modified McMillan semiempirical equation used to calculate T_c (Figure S2).

To better quantify the way in which QNEs affect each structure, we calculate the mean atomic displacements they impose as

$$\Delta X = \sum_a^{N_A} \frac{|\mathbf{R}_q^a - \mathbf{R}_c^a|}{N_A}, \quad (1)$$

where \mathbf{R}_q^a is the quantum anharmonic position calculated for atom a , \mathbf{R}_c^a is the position of the same atom as obtained from the minimum of the BOES, and N_A represents the number of atoms in the unit cell. Figure 5 plots the percentage change in $\alpha^2 F$ in going from the static to the quantum lattice as a function of ΔX . It is clear that $\alpha^2 F$ can change dramatically, even when ΔX does not. For the Type I structures, which are represented by full symbols, though the structure remains practically unaltered after the introduction of QNEs, a reduction for $\alpha^2 F$ is observed, implying a decreased T_c . For the Type II systems, represented by the empty symbols, the exact opposite is observed: the introduction of QNEs modifies the atomic parameters such that $\Delta X > 0$ and T_c is increased. This analysis reveals that a comparison of the optimized geometries obtained assuming classic and quantum nuclei is sufficient to predict the way in which QNEs will affect the superconducting properties of hydrides. Our findings align with the analysis performed by Lucrezi *et al.* on LaBH_8 ⁴⁷, who concluded that QNEs give rise to two general phenomena that affect superconducting properties: one driven by structural changes and another related to phonon-phonon interactions resulting from anharmonicity. Type I systems include those where the renormalization of the phonon-phonon interactions dominates over the structural perturbations, while the opposite phenomenon is characteristic of Type II compounds.

However, to obtain $\alpha^2 F$ or ΔX a full geometry optimization and calculation of the phonon band structure and the EPC strength for both the classic and quantum lattice, the latter being particularly expensive even when accelerated using machine learning interatomic potentials, is still required.

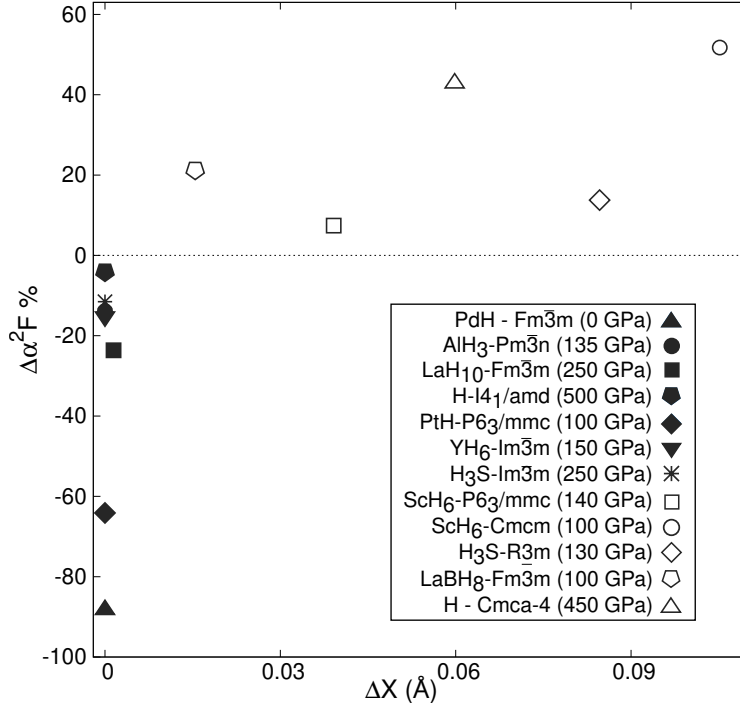


Figure 5: The amount by which the integral of the Eliashberg spectral function ($\alpha^2F = \int_0^\infty \alpha^2F(\omega)d\omega$) differs, given as a percentage, between calculations that treat the nuclei as quantum particles versus classical particles, as a function of the mean atomic displacement, ΔX , defined in Equation (1). As shown in the legend, filled (open) symbols correspond to Type I (Type II) structures.

What we desire is a descriptor that predicts the way in which QNEs affect the geometric and superconducting properties of a structure that can be obtained knowing *only* the geometry of the classic lattice. One might be tempted to conclude that crystals with higher symmetries are likely to be perturbed less by QNEs than ones with lower symmetries. However, such a rule of thumb would be incorrect, as the structurally LaH₁₀ (Type I) and LaBH₈ (Type II) compounds both assume the $Fm\bar{3}m$ spacegroup. Another example where spacegroups would not help differentiate between the two types of systems is PtH and ScH₆ at 140 GPa, which both adopt $P6_3/mmc$ symmetry, the former a member of the Type I family and the latter a member of Type II.

Since the total number of symmetry operations of the spacegroup and the total number of free parameters in its Wyckoff sites is insufficient to predict *a priori* how QNEs will impact a structure, another metric must be found. Because our observations suggested that the local bonding

environments about the atoms in a phase are key for predicting how it will be affected by QNEs, we first considered the vector weighted sum of the interatomic distances about an atom, and the Crystal Orbital Hamilton Population integrated to E_F (iCOHP)⁹⁶ between atom pairs, both summed over the unit cell, as descriptors (Table S6 and S7). However, neither approach demonstrated sufficient predictive power. Analyzing interatomic distances alone is insufficient because while one distance might correspond to a value typical of a single bond for one atom pair, for another atom pair it may be typical of a non-bonding or even a repulsive interaction. Though the iCOHP is sensitive to the bond strength, our tests showed that it was not able to predict which class LaH₁₀ and H-*Cmca*-4 would fall into (Table S6).

However, as shown below, an analysis of the local interatomic bonding patterns as calculated via the integral of the crystal orbital bonding index (iCOBI)⁴⁹ for pairs of atoms resulted in a predictive and simple-to-use descriptor. The iCOBI is a generalization of the bond index according to Wiberg and Mayer, which is directly related to the classic bond order, adapted to periodic systems. For a single bond, such as between two carbon atoms in diamond, an iCOBI of 1 would be expected, whereas in an ionic system, such as between the Na⁺ and Cl⁻ atoms in the rocksalt phase, iCOBI should be near 0. Previous computations yielded 0.95 and 0.09 for these cases⁴⁹, in-line with our expectations. In a mixed covalent and ionic system, a value between 0 and 1 is therefore likely to be found.

In the high pressure hydrides the interaction between hydrogen atoms is expected to yield iCOBIs that fall between 1 (for an H₂ molecule) and 0 (between hydridic hydrogen, H⁻, or atomic hydrogen, H, and any other hydrogenic motif). When *p*-block elements form weak covalent bonds with the hydrogen atoms, such as in H₃S, the iCOBI is expected to be notably larger than 0, but smaller than 1. For example, in *Im* $\bar{3}m$ H₃S at 270 GPa the iCOBI between the S and H atoms was computed to be 0.34, indicating a bond order of roughly 1/3⁹⁷. While the interaction between electropositive elements and hydrogen is expected to be primarily ionic, we note that covalent (dative) interactions such as those arising from donation of orbitals from bonding states to a vacant d-orbital on the metal atom and back-bonding from an occupied metal d-orbital to antibonding

hydrogenic states (*e.g.* $\text{H}_2 \sigma \rightarrow \text{metal d}$, and $\text{metal d} \rightarrow \text{H}_2 \sigma^*$)⁹³⁻⁹⁵ are likely to be non-negligible resulting in non-zero iCOBIs. Importantly, we hypothesized that as long as the individual iCOBIs are not equal to naught, a vector sum of them about an atom can provide information about the symmetry of the atom’s local bonding environment.

To test this hypothesis, we first introduced a vector quantity, \mathbf{V}_x , computed for each atom x . This vector is the sum of the iCOBI values for all of the interactions between an atom and its neighboring atoms α ($\text{iCOBI}(x, \alpha)$) weighted by a unit vector, $\mathbf{i}_{x\alpha}$, which denotes the direction of each interaction. This summation is performed over all neighbors for which the iCOBI values fall above a user-defined threshold, and divided by the number of interactions considered, B_x , as

$$\mathbf{V}_x = \frac{1}{B_x} \sum_{\alpha=1}^{B_x} \text{iCOBI}(x, \alpha) \mathbf{i}_{x\alpha}. \quad (2)$$

The vector \mathbf{V}_x , is able to capture the asymmetry of the local bonding environment around the atom x and quantify the effect of QNEs on the structure. However, \mathbf{V}_x exhibits redundancy due to the symmetry of the system: atoms located on equivalent Wyckoff positions are expected to have identical magnitudes of \mathbf{V}_x . To simplify the analysis and reduce the number of variables, we investigated $S_x = |\mathbf{V}_x|$ for just one of the atoms belonging to the same Wyckoff position. We defined this magnitude as the symmetry index or parameter, denoted as S_a , where a represents the group of atoms x in the same Wyckoff position. The symmetry index is expected to be very small or zero for an atom that is in a completely symmetric bonding environment, whereas larger values of S_a correlate with a greater degree of local bonding asymmetry around the atom.

Is it possible to distinguish Type I structures from Type II based on the value of the symmetry parameters calculated for each symmetry inequivalent atom in the optimized classic lattice, S_a^c ? And, would the symmetry parameters for quantum nuclei, S_a^q , differ for these two classes of compounds? To answer these questions, S_a^c and S_a^q were calculated for each distinct atom in the systems illustrated in Figures 1 and 2, and the results are provided in Table 1. The analysis was performed using a cutoff threshold of 0.05 for the iCOBI in the calculation of \mathbf{V}_x (Equation 2). This threshold was

chosen to prioritize the most significant interactions and to minimize the inclusion of artifacts resulting from incomplete wavefunction projections onto localized orbitals. These interactions are reported in Tables S4 and S5.

Table 1: The symmetry inequivalent atoms and their Wyckoff positions in the Type I (Figure 1) and Type II (Figure 2) structures along with the corresponding symmetry index computed treating the nuclei as classical, S_a^c , and quantum, S_a^q , objects. The Wyckoff parameters given in parenthesis for $\text{ScH}_6 - Cmc$ correspond to the positions of these atoms in the higher symmetry $\text{ScH}_6 - P6_3/mmc$ phase.

Structure	Atom	Wyckoff letter	S_a^c	S_a^q
Type I				
PdH - $Fm\bar{3}m$ (1 atm)	Pd	4a	0	0
	H	4b	0	0
AlH ₃ - $Pm\bar{3}m$ (135 GPa)	Al	2a	0	0
	H	6c	0	0
LaH ₁₀ - $Fm\bar{3}m$ (250 GPa)	La	4b	0	0
	H	8c	0	0
	H	32f	0.009	0.009
H - $I4_1/amd$ (500 GPa)	H	4b	0	0
PtH - $P6_3/mmc$ (100 GPa)	Pt	2d	0	0
	H	2a	0	0
YH ₆ - $Im\bar{3}m$ (150 GPa)	Y	2a	0	0
	H	12d	0	0
H ₃ S - $Im\bar{3}m$ (250 GPa)	S	2a	0	0
	H	6b	0	0
Type II				
ScH ₆ - $P6_3/mmc$ (140 GPa)	Sc	2d	0	0
	H	12k	0.056	0.054
ScH ₆ - Cmc (100 GPa)	Sc	4c	0.012	0 (2d)
	H	16h	0.040	0.055 (12k)
	H	8f	0.082	0.055 (12k)
H ₃ S - $R\bar{3}m$ (130 GPa)	S	3a	0.076	0
	H	9b	0.116	0
LaBH ₈ - $Fm\bar{3}m$ (100 GPa)	La	4b	0	0
	B	4a	0	0
	H	32f	0.062	0.063
H - $Cmca-4$ (450 GPa)	H	8f	0.022	0.014

Examination of Table 1 clearly shows that for Type I structures both the classic and quantum asymmetry parameters are the same and are either zero, or very nearly zero, for each symmetry inequivalent atom. In fact, the only non-zero value that was calculated was for the hydrogen atoms at the 32f Wyckoff position in LaH₁₀, which has a free parameter. In the lattice optimized with QNEs, this value does not change, in-line with the above discussion where it was shown that the quantum nature of the hydrogen atoms and the resulting anharmonicity had a negligible effect on the optimized atomic positions. The value of S_a^c for this Wyckoff position, 0.009, is an order of magnitude smaller than the non-zero values computed for any of the Type II structures. Thus, we suggest that the classical lattice symmetry index, S_a^c , should be less than or equal to 0.01 for every atom within hydrides that belong to the Type I family, that is those where QNEs do not alter the structure, but where the phonon modes are shifted to higher frequencies because of the phonon-phonon interactions. These combined effects reduce λ , as well as $\alpha^2 F$, leading to a concomitant decrease in T_c in Type I systems. Our analysis rationalizes why LaH₁₀ belongs to the Type I family: despite the intrinsic freedom of the 32f Wyckoff site, the local bonding environment about these atoms is sufficiently symmetric to ensure that the atomic positions are not strongly altered by QNEs.

For Type II structures, on the other hand, at least one of the symmetry inequivalent atoms possesses a significant S_a^c . Interestingly, the symmetry parameters for all but two of the heavy atoms are zero, in-line with the finding that QNEs do not perturb their positions during the relaxation, such that S_a^q is also zero. The two exceptions are the Sc atoms within ScH₆-*Cmcm* and the S atoms within H₃S-*R3m*, where the classical symmetry indices of 0.022 and 0.076, respectively, decreased to zero during structural relaxation with the SSCHA, resulting in a symmetric environment about these atoms. In-line with the expectation that the lighter hydrogen atoms should have a higher proclivity to be perturbed by QNEs than the heavy atoms, they had significantly larger S_a^c values (0.046 - 0.852), which all decreased substantially when their lattices were optimized with the SSCHA.

These results highlight that the iCOBI based symmetry parameter is an excellent descriptor for identifying the atoms that will be most affected by QNEs in hydrogen rich materials including those

that are stable at low and at high pressures. Moreover, we can conclude that compounds with at least one large S_a^c value tend to increase the symmetry in their local bonding environment upon structural relaxation with QNEs, in particular around the hydrogen atoms, shifting the phonon modes to lower frequencies. These effects serve to increase λ , as well as α^2F , and the concomitant T_c , in stark contrast to what is observed in Type I systems.

Conclusions

This work investigates how quantum nuclear effects (QNEs) and the anharmonicity they can induce alter the structural and superconducting properties of hydrogen-based superconductors. We introduce a symmetry bonding index or parameter, S_a , for each symmetry inequivalent atom, which is based upon a vector weighted sum of the integrated crystal orbital bonding indices (iCOBIs) between this atom and others falling above a user-defined threshold (here chosen as iCOBI=0.05). An S_a value of zero corresponds to an atom in a nearly perfect symmetric bonding configuration, whereas larger values of S_a are associated with non-negligible deviations from ideal symmetry. This index can be computed for lattices of classical nuclei optimized within the Born-Oppenheimer approximation, S_a^c , as well as relaxations that treat the nuclei quantum mechanically, S_a^q . Importantly, we find that the classical results are sufficient to predict the way in which QNEs will impact the properties of both ambient pressure and high pressure hydride superconductors. Thus, S_a^c , which can be calculated knowing only the positions of the classical lattice, is a robust and quick-to-compute descriptor that can predict how QNEs and anharmonicity affect the geometry of a compound and its superconducting behavior.

Two families of structures were identified and analyzed. In Type I systems S_a^c was calculated to be zero for most atom types, and we suggest that it should not exceed 0.01 for any atom belonging to phases in this class. QNEs do not perturb the geometries of Type I compounds, but anharmonicity lowers the pressure at which they are predicted to become dynamically unstable, with a consequent blue shift of their phonon spectra, which is stronger for the lower optical branches. This perturbation

of the phonon modes results in a decrease of the T_c . In Type II systems, on the other hand, S_a^c is large for at least one of the symmetry inequivalent atoms, meaning that these phases have a lower degree of local bonding symmetry. Structural relaxation with QNEs attempts to restore the local symmetry, often (but not always) resulting in smaller S_a^q values. This geometric perturbation of the quantum lattice destabilizes the structure, softens the phonon modes, and enhances T_c , sometimes by an impressive factor of 2-4 when QNEs increase the density of states at the Fermi level. We expect the introduced classical asymmetry parameter will become a powerful tool in the *a priori* prediction of the effect of QNEs on the geometries, phonon modes and critical temperatures of hydride superconductors, and its quantum counterpart will be used to understand the magnitude of these effects for specific lattices and atom types.

Supporting Information

The Supporting Information is available free of charge on the ACS Publication website. It includes: the electronic configurations of the PAW potentials used in the LOBSTER calculations, the unit cell parameters and atomic positions for all of the structures optimized in the Born-Oppenheimer approximations, tables listing the classical and quantum λ , ω_{\log} and T_c , plots of the quantum versus the classical λ and ω_{\log} , the values of the most relevant bonds used in the iCOBI analysis, and the data for the analysis performed with iCOHPs and interatomic distances.

Acknowledgments

Funding for this research is provided by the National Science Foundation, under award DMR-2136038 and the European Research Council (ERC) under the European Union's Horizon 2020 research and innovation program (Grant Agreement No. 802533). I.E. also acknowledges financial support from the Department of Education, Universities and Research of the Eusko Jaurlaritza, and the University of the Basque Country UPV/EHU (Grant No. IT1527-22); and the Spanish Ministerio

de Ciencia e Innovación (Grant No. PID2022-142861NA-I00). Calculations were performed at the Center for Computational Research at SUNY Buffalo (<http://hdl.handle.net/10477/79221>).

References

- (1) Ashcroft, N. W. Metallic Hydrogen: A High-Temperature Superconductor? *Phys. Rev. Lett.* **1968**, *21*, 1748–1749.
- (2) Ashcroft, N. W. Hydrogen Dominant Metallic Alloys: High Temperature Superconductors? *Phys. Rev. Lett.* **2004**, *92*, 187002.
- (3) Drozdov, A. P.; Eremets, M. I.; Troyan, I. A.; Ksenofontov, V.; Shylin, S. I. Conventional Superconductivity at 203 Kelvin at High Pressures in the Sulfur Hydride System. *Nature* **2015**, *525*, 73–76.
- (4) Somayazulu, M.; Ahart, M.; Mishra, A. K.; Geballe, Z. M.; Baldini, M.; Meng, Y.; Struzhkin, V. V.; Hemley, R. J. Evidence for Superconductivity Above 260 K in Lanthanum Superhydride at Megabar Pressures. *Phys. Rev. Lett.* **2019**, *122*, 027001 (1–6).
- (5) Drozdov, A. P.; Kong, P. P.; Minkov, V. S.; Besedin, S. P.; Kuzovnikov, M. A.; Mozaffari, S.; Balicas, L.; Balakirev, F. F.; Graf, D. E.; Prakapenka, V. B.; Greenberg, E.; Knyazev, D. A.; Tkacz, M.; Eremets, M. I. Superconductivity at 250 K in Lanthanum Hydride Under High Pressures. *Nature* **2019**, *569*, 528–531.
- (6) Shao, M.; Chen, W.; Zhang, K.; Huang, X.; Cui, T. High-Pressure Synthesis of Superconducting Clathrate Like YH_4 . *Phys. Rev. B* **2021**, *104*, 174509 (1–6).
- (7) Troyan, I. A. et al. Anomalous High-temperature Superconductivity in YH_6 . *Adv. Mater.* **2021**, *33*, 2006832.
- (8) Kong, P.; Minkov, V. S.; Kuzovnikov, M. A.; Drozdov, A. P.; Besedin, S. P.; Mozaffari, S.; Balicas, L.; Balakirev, F. F.; Prakapenka, V. B.; Chariton, S.; Knyazev, D. A.; Greenberg, E.;

- Eremets, M. I. Superconductivity up to 243 K in the Yttrium-Hydrogen System Under High Pressure. *Nat. Commun.* **2021**, *12*, 5075 (1–9).
- (9) Ma, L.; Wang, K.; Xie, Y.; Yang, X.; Wang, Y.; Zhou, M.; Liu, H.; Yu, X.; Zhao, Y.; Wang, H.; Liu, G.; Ma, Y. High-Temperature Superconducting Phase in Clathrate Calcium Hydride CaH₆ up to 215 K at a Pressure of 172 GPa. *Phys. Rev. Lett.* **2022**, *128*, 167001 (1–6).
- (10) Li, Z. et al. Superconductivity Above 200 K Discovered in Superhydrides of Calcium. *Nat. Commun.* **2022**, *13*, 2863 (1–5).
- (11) Semenok, D. V. et al. Superconductivity at 253 K in Lanthanum-Yttrium Ternary Hydrides. *Mater. Today* **2021**, *48*, 18–28.
- (12) Song, Y.; Bi, J.; Nakamoto, Y.; Shimizu, K.; Liu, H.; Zou, B.; Liu, G.; Wang, H.; Ma, Y. Stoichiometric Ternary Superhydride LaBeH₈ as a New Template for High-Temperature Superconductivity at 110 K Under 80 GPa. *Phys. Rev. Lett.* **2023**, *130*, 266001 (1–8).
- (13) Chen, W.; Huang, X.; Semenok, D. V.; Chen, S.; Zhou, D.; Zhang, K.; Oganov, A. R.; Cui, T. Enhancement of Superconducting Properties in the La–Ce–H System at Moderate Pressures. *Nat. Commun.* **2023**, *14*, 2660 (1–8).
- (14) Chen, L.-C.; Luo, T.; Cao, Z.-Y.; Dalladay-Simpson, P.; Huang, G.; Peng, D.; Zhang, L.-L.; Gorelli, F. A.; Zhong, G.-H.; Lin, H.-Q.; Chen, X.-J. Synthesis and Superconductivity in Yttrium-Cerium Hydrides at High Pressures. *Nat. Commun.* **2024**, *15*, 1809 (1–7).
- (15) Flores-Livas, J. A.; Boeri, L.; Sanna, A.; Profeta, G.; Arita, R.; Eremets, M. A Perspective on Conventional High-Temperature Superconductors at High Pressure: Methods and Materials. *Phys. Rep.* **2020**, *856*, 1–78.
- (16) Pickard, C. J.; Errea, I.; Eremets, M. I. Superconducting Hydrides Under Pressure. *Annu. Rev. Condens. Matter Phys.* **2020**, *11*, 57–76.

- (17) Bi, T.; Zarifi, N.; Terpstra, T.; Zurek, E. In *Reference Module in Chemistry, Molecular Sciences and Chemical Engineering*; Reedijk, J., Ed.; Elsevier: Waltham, MA, 2019; pp 1–36.
- (18) Duan, D.; Liu, Y.; Tian, F.; Li, D.; Huang, X.; Zhao, Z.; Yu, H.; Liu, B.; Tian, W.; Cui, T. Pressure-Induced Metallization of Dense $(\text{H}_2\text{S})_2\text{H}_2$ with High- T_c Superconductivity. *Sci. Rep.* **2014**, *4*, 1–6.
- (19) Duan, D.; Huang, X.; Tian, F.; Li, D.; Yu, H.; Liu, Y.; Ma, Y.; Liu, B.; Cui, T. Pressure-Induced Decomposition of Solid Hydrogen Sulfide. *Phys. Rev. B* **2015**, *91*, 180502.
- (20) Liu, H.; Li, Y.; Gao, G.; Tse, J. S.; Naumov, I. I. Crystal Structure and Superconductivity of PH_3 at High Pressures. *J. Phys. Chem. C* **2016**, *120*, 3458–3461.
- (21) Peng, F.; Sun, Y.; Pickard, C. J.; Needs, R. J.; Wu, Q.; Ma, Y. Hydrogen Clathrate Structures in Rare Earth Hydrides at High Pressures: Possible Route to Room-Temperature Superconductivity. *Phys. Rev. Lett.* **2017**, *119*, 107001.
- (22) Liu, H.; Naumov, I. I.; Hoffmann, R.; Ashcroft, N. W.; Hemley, R. J. Potential High- T_c Superconducting Lanthanum and Yttrium Hydrides at High Pressure. *Proc. Natl. Acad. Sci. U.S.A.* **2017**, *114*, 6990–6995.
- (23) Semenok, D. V.; Kruglov, I. A.; Savkin, I. A.; Kvashnin, A. G.; Oganov, A. R. On Distribution of Superconductivity in Metal Hydrides. *Curr. Opin. Solid State Mater. Sci.* **2020**, *24*, 100808.
- (24) Belli, F.; Novoa, T.; Contreras-García, J.; Errea, I. Strong Correlation Between Electronic Bonding Network and Critical Temperature in Hydrogen-Based Superconductors. *Nat. Comm.* **2021**, *12*, 1–11.
- (25) Kokail, C.; Von Der Linden, W.; Boeri, L. Prediction of High- T_c Conventional Superconductivity in the Ternary Lithium Borohydride System. *Phys. Rev. Mater.* **2017**, *1*, 074803.

- (26) Saha, S.; Di Cataldo, S.; Amsler, M.; Von Der Linden, W.; Boeri, L. High-Temperature Conventional Superconductivity in the Boron-Carbon System: Material Trends. *Phys. Rev. B* **2020**, *102*, 024519.
- (27) Sun, Y.; Lv, J.; Xie, Y.; Liu, H.; Ma, Y. Route to a Superconducting Phase Above Room Temperature in Electron-Doped Hydride Compounds Under High Pressure. *Phys. Rev. Lett.* **2019**, *123*, 097001.
- (28) Di Cataldo, S.; von der Linden, W.; Boeri, L. First-Principles Search of Hot Superconductivity in La-XH Ternary Hydrides. *npj Comput. Mater.* **2022**, *8*, 1–8.
- (29) Lucrezi, R.; Di Cataldo, S.; von der Linden, W.; Boeri, L.; Heil, C. In-Silico Synthesis of Lowest-Pressure High- T_c Ternary Superhydrides. *npj Comput. Mater.* **2022**, *8*, 119.
- (30) Di Cataldo, S.; Heil, C.; von der Linden, W.; Boeri, L. LaBH_8 : Towards High- T_c Low-Pressure Superconductivity in Ternary Superhydrides. *Phys. Rev. B* **2021**, *104*, L020511.
- (31) Liang, X.; Bergara, A.; Wei, X.; Song, X.; Wang, L.; Sun, R.; Liu, H.; Hemley, R. J.; Wang, L.; Gao, G.; Tian, Y. Prediction of High- T_c Superconductivity in Ternary Lanthanum Borohydrides. *Phys. Rev. B* **2021**, *104*, 134501.
- (32) Zurek, E.; Bi, T. High-Temperature Superconductivity in Alkaline and Rare Earth Polyhydrides at High Pressure: A Theoretical Perspective. *J. Chem. Phys.* **2019**, *150*, 050901 (1–13).
- (33) Errea, I.; Belli, F.; Monacelli, L.; Sanna, A.; Koretsune, T.; Tadano, T.; Bianco, R.; Calandra, M.; Arita, R.; Mauri, F.; Flores-Livas, J. A. Quantum Crystal Structure in the 250-Kelvin Superconducting Lanthanum Hydride. *Nature* **2020**, *578*, 66–69.
- (34) Errea, I.; Calandra, M.; Pickard, C. J.; Nelson, J. R.; Needs, R. J.; Li, Y.; Liu, H.; Zhang, Y.; Ma, Y.; Mauri, F. Quantum Hydrogen-Bond Symmetrization in the Superconducting Hydrogen Sulfide System. *Nature* **2016**, *532*, 81–84.

- (35) Liu, H.; Naumov, I. I.; Geballe, Z. M.; Somayazulu, M.; Tse, J. S.; Hemley, R. J. Dynamics and Superconductivity in Compressed Lanthanum Superhydride. *Phys. Rev. B* **2018**, *98*, 100102.
- (36) Hou, P.; Belli, F.; Bianco, R.; Errea, I. Strong Anharmonic and Quantum Effects in $\text{Pm}\bar{3}n$ AlH_3 Under High Pressure: A First-Principles Study. *Phys. Rev. B* **2021**, *103*, 134305 (1–8).
- (37) Hou, P.; Belli, F.; Bianco, R.; Errea, I. Quantum Anharmonic Enhancement of Superconductivity in $P6_3/mmc$ ScH_6 at High Pressures: A First-Principles Study. *J. Appl. Phys.* **2021**, *130*, 175902.
- (38) Geng, N.; Hilleke, K. P.; Belli, F.; Das, P. K.; Zurek, E. Superconductivity in CH_4 and BH_4^- Containing Compounds Derived From the High-Pressure Superhydrides. *Mater. Today Phys.* **2024**, *44*, 101443.
- (39) Errea, I.; Calandra, M.; Mauri, F. First-Principles Theory of Anharmonicity and the Inverse Isotope Effect in Superconducting Palladium-Hydride Compounds. *Phys. Rev. Lett.* **2013**, *111*, 177002.
- (40) Belli, F.; Zurek, E. Efficient Modelling of Anharmonicity and Quantum Effects in PdCuH_2 with Machine Learning Potentials. *arXiv preprint arXiv:2406.13178* **2024**,
- (41) Errea, I.; Calandra, M.; Mauri, F. Anharmonic Free Energies and Phonon Dispersions From the Stochastic Self-Consistent Harmonic Approximation: Application to Platinum and Palladium Hydrides. *Phys. Rev. B* **2014**, *89*, 064302 (1–16).
- (42) Bianco, R.; Errea, I.; Paulatto, L.; Calandra, M.; Mauri, F. Second-Order Structural Phase Transition, Free Energy Curvature, and Temperature-dependent Anharmonic Phonons in the Self-Consistent Harmonic Approximation: Theory and Stochastic Implementation. *Phys. Rev. B* **2017**, *96*, 014111 (1–26).
- (43) Monacelli, L.; Errea, I.; Calandra, M.; Mauri, F. Pressure and Stress Tensor of Complex

- Anharmonic Crystals Within the Stochastic Self-Consistent Harmonic Approximation. *Phys. Rev. B* **2018**, *98*, 024106 (1–17).
- (44) Monacelli, L.; Bianco, R.; Cherubini, M.; Calandra, M.; Errea, I.; Mauri, F. The Stochastic Self-Consistent Harmonic Approximation: Calculating Vibrational Properties of Materials with Full Quantum and Anharmonic Effects. *J. Phys. Cond. Matt.* **2021**, *33*, 363001 (1–34).
- (45) Monacelli, L.; Mauri, F. Time-Dependent Self-Consistent Harmonic Approximation: Anharmonic Nuclear Quantum Dynamics and Time Correlation Functions. *Phys. Rev. B* **2021**, *103*, 104305.
- (46) Ranalli, L.; Verdi, C.; Monacelli, L.; Kresse, G.; Calandra, M.; Franchini, C. Temperature-Dependent Anharmonic Phonons in Quantum Paraelectric KTaO_3 by First Principles and Machine-Learned Force Fields. *Adv. Quantum Technol.* **2023**, *6*, 2200131.
- (47) Lucrezi, R.; Kogler, E.; Di Cataldo, S.; Aichhorn, M.; Boeri, L.; Heil, C. Quantum Lattice Dynamics and Their Importance in Ternary Superhydride Clathrates. *Commun. Phys.* **2023**, *6*, 298.
- (48) Belli, F.; Errea, I. Impact of Ionic Quantum Fluctuations on the Thermodynamic Stability and Superconductivity of LaBH_8 . *Phys. Rev. B* **2022**, *106*, 134509 (1–10).
- (49) Müller, P. C.; Ertural, C.; Hempelmann, J.; Dronskowski, R. Crystal Orbital Bond Index: Covalent Bond Orders in Solids. *J. Phys. Chem. C* **2021**, *125*, 7959–7970.
- (50) Errea, I.; Belli, F.; Monacelli, L.; Sanna, A.; Koretsune, T.; Tadano, T.; Bianco, R.; Calandra, M.; Arita, R.; Mauri, F.; Flores-Livas, J. A. Quantum Crystal Structure in the 250 Kelvin Superconducting Lanthanum Hydride. *Nature* **2020**, *578*, 66–69.
- (51) Borinaga, M.; Errea, I.; Calandra, M.; Mauri, F.; Bergara, A. Anharmonic Effects in Atomic Hydrogen: Superconductivity and Lattice Dynamical Stability. *Phys. Rev. B* **2016**, *93*, 174308.

- (52) Borinaga, M.; Riego, P.; Leonardo, A.; Calandra, M.; Mauri, F.; Bergara, A.; Errea, I. Anharmonic Enhancement of Superconductivity in Metallic Molecular $Cmca\bar{4}$ Hydrogen at High Pressure: A First-Principles Study. *J. Phys. Condens. Matter* **2016**, *28*, 494001.
- (53) Giannozzi, P. et al. QUANTUM ESPRESSO: A Modular and Open-Source Software Project for Quantum Simulations of Materials. *J. Phys. Condens. Matter* **2009**, *21*, 395502.
- (54) Giannozzi, P. et al. Advanced Capabilities for Materials Modelling with Quantum ESPRESSO. *J. Phys. Condens. Matter* **2017**, *29*, 465901.
- (55) Perdew, J. P.; Burke, K.; Ernzerhof, M. Generalized Gradient Approximation Made Simple. *Phys. Rev. Lett.* **1996**, *77*, 3865.
- (56) Baroni, S.; De Gironcoli, S.; Dal Corso, A.; Giannozzi, P. Phonons and Related Crystal Properties From Density-Functional Perturbation Theory. *Rev. Mod. Phys.* **2001**, *73*, 515.
- (57) Allen, P. B.; Mitrovic, B. In *Theory of Superconducting T_c* ; Ehrenreich, H., Seitz, F., Turnbull, D., Eds.; Solid State Phys.; Academic Press, 1983; Vol. 37; pp 1–92.
- (58) Hafner, J. Ab-Initio Simulations of Materials Using VASP: Density-Functional Theory and Beyond. *J. Comput. Chem.* **2008**, *29*, 2044–2078.
- (59) Blöchl, P. E. Projector Augmented-Wave Method. *Phys. Rev. B* **1994**, *50*, 17953–17979.
- (60) Monkhorst, H. J.; Pack, J. D. Special Points for Brillouin-Zone Integrations. *Phys. Rev. B* **1976**, *13*, 5188–5192.
- (61) Nelson, R.; Ertural, C.; George, J.; Deringer, V. L.; Hautier, G.; Dronskowski, R. LOBSTER: Local Orbital Projections, Atomic Charges, and Chemical-Bonding Analysis From Projector-Augmented-Wave-Based Density-Functional Theory. *J. Comput. Chem.* **2020**, *41*, 1931–1940.
- (62) Jena, P.; Jones, J.; Nieminen, R. M. Effect of Zero-Point Motion on the Superconducting Transition Temperature of PdH(D). *Phys. Rev. B* **1984**, *29*, 4140–4143.

- (63) Schirber, J. E.; Morosin, B. Lattice Constants of $\beta - \text{PdH}_x$ and $\beta - \text{PdD}_x$ with x Near 1.0. *Phys. Rev. B* **1975**, *12*, 117–118.
- (64) Elsässer, C.; Ho, K. M.; Chan, C. T.; Fähnle, M. Vibrational States for Hydrogen in Palladium. *Phys. Rev. B* **1991**, *44*, 10377–10380.
- (65) Klein, B. M.; Economou, E. N.; Papaconstantopoulos, D. A. Inverse Isotope Effect and the x Dependence of the Superconducting Transition Temperature in PdH_x and PdD_x . *Phys. Rev. Lett.* **1977**, *39*, 574–577.
- (66) Miller, R. J.; Satterthwaite, C. B. Electronic Model for the Reverse Isotope Effect in Superconducting Pd-H(D). *Phys. Rev. Lett.* **1975**, *34*, 144–148.
- (67) Schirber, J.; Northrup Jr, C. Concentration Dependence of the Superconducting Transition Temperature in PdH_x and PdD_x . *Phys. Rev. B* **1974**, *10*, 3818.
- (68) Stritzker, B.; Buckel, W. Superconductivity in the Palladium-Hydrogen and the Palladium-Deuterium Systems. *Z. Phys. A* **1972**, *257*, 1–8.
- (69) Pickard, C. J.; Needs, R. J. Metallization of Aluminum Hydride at High Pressures: A First-Principles Study. *Phys. Rev. B* **2007**, *76*, 144114.
- (70) Goncharenko, I.; Erements, M. I.; Hanfland, M.; Tse, J. S.; Amboage, M.; Yao, Y.; Trojan, I. A. Pressure-Induced Hydrogen-Dominant Metallic State in Aluminum Hydride. *Phys. Rev. Lett.* **2008**, *100*, 045504.
- (71) Rousseau, B.; Bergara, A. Giant Anharmonicity Suppresses Superconductivity in AlH_3 Under Pressure. *Phys. Rev. B* **2010**, *82*, 104504.
- (72) McMahon, J. M.; Ceperley, D. M. High-Temperature Superconductivity in Atomic Metallic Hydrogen. *Phys. Rev. B* **2011**, *84*, 144515.
- (73) Monacelli, L.; Casula, M.; Nakano, K.; Sorella, S.; Mauri, F. Quantum Phase Diagram of High-Pressure Hydrogen. *Nat. Phys.* **2023**, *19*, 845–850.

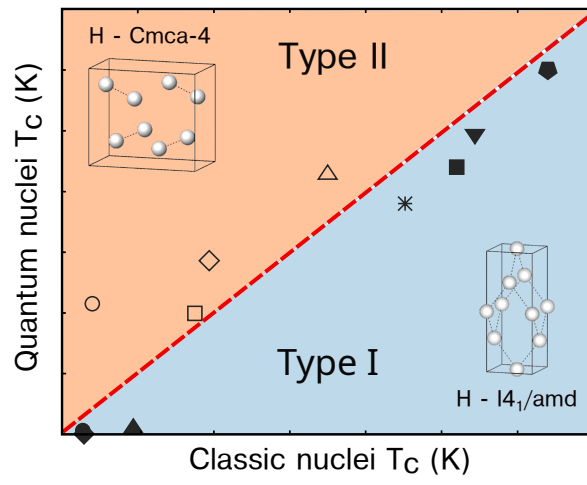
- (74) Azadi, S.; Monserrat, B.; Foulkes, W. M. C.; Needs, R. J. Dissociation of High-Pressure Solid Molecular Hydrogen: A Quantum Monte Carlo and Anharmonic Vibrational Study. *Phys. Rev. Lett.* **2014**, *112*, 165501.
- (75) McMinis, J.; Clay, R. C.; Lee, D.; Morales, M. A. Molecular to Atomic Phase Transition in Hydrogen Under High Pressure. *Phys. Rev. Lett.* **2015**, *114*, 105305.
- (76) Scheler, T.; Degtyareva, O.; Marqués, M.; Guillaume, C. L.; Proctor, J. E.; Evans, S.; Gregoryanz, E. Synthesis and Properties of Platinum Hydride. *Phys. Rev. B* **2011**, *83*, 214106.
- (77) Kim, D. Y.; Scheicher, R. H.; Pickard, C. J.; Needs, R. J.; Ahuja, R. Predicted Formation of Superconducting Platinum-Hydride Crystals Under Pressure in the Presence of Molecular Hydrogen. *Phys. Rev. Lett.* **2011**, *107*, 117002.
- (78) Zhou, X.-F.; Oganov, A. R.; Dong, X.; Zhang, L.; Tian, Y.; Wang, H.-T. Superconducting High-Pressure Phase of Platinum Hydride From First Principles. *Phys. Rev. B* **2011**, *84*, 054543.
- (79) Heil, C.; Di Cataldo, S.; Bachelet, G. B.; Boeri, L. Superconductivity in Sodalite-Like Yttrium Hydride Clathrates. *Phys. Rev. B* **2019**, *99*, 220502.
- (80) Ye, X.; Zarifi, N.; Zurek, E.; Hoffmann, R.; Ashcroft, N. W. High Hydrides of Scandium Under Pressure: Potential Superconductors. *J. Phys. Chem. C* **2018**, *122*, 6298–6309.
- (81) Duan, D.; Liu, Y.; Tian, F.; Li, D.; Huang, X.; Zhao, Z.; Yu, H.; Liu, B.; Tian, W.; Cui, T. Pressure-Induced Metallization of Dense $(\text{H}_2\text{S})_2\text{H}_2$ with High- T_c Superconductivity. *Sci. Rep.* **2014**, *4*, 6968.
- (82) Duan, D.; Huang, X.; Tian, F.; Li, D.; Yu, H.; Liu, Y.; Ma, Y.; Liu, B.; Cui, T. Pressure-Induced Decomposition of Solid Hydrogen Sulfide. *Phys. Rev. B* **2015**, *91*, 180502.
- (83) Einaga, M.; Sakata, M.; Ishikawa, T.; Shimizu, K.; Eremets, M. I.; Drozdov, A. P.; Troyan, I. A.;

- Hirao, N.; Ohishi, Y. Crystal Structure of the Superconducting Phase of Sulfur Hydride. *Nat. Phys.* **2016**, *12*, 835–838.
- (84) Errea, I.; Calandra, M.; Pickard, C. J.; Nelson, J.; Needs, R. J.; Li, Y.; Liu, H.; Zhang, Y.; Ma, Y.; Mauri, F. High-Pressure Hydrogen Sulfide From First Principles: A Strongly Anharmonic Phonon-Mediated Superconductor. *Phys. Rev. Lett.* **2015**, *114*, 157004.
- (85) Di Cataldo, S.; Heil, C.; von der Linden, W.; Boeri, L. LaBH₈: Towards High-T_c Low-Pressure Superconductivity in Ternary Superhydrides. *Phys. Rev. B* **2021**, *104*, L020511.
- (86) Zhang, Z.; Cui, T.; Hutcheon, M. J.; Shipley, A. M.; Song, H.; Du, M.; Kresin, V.; Duan, D.; Pickard, C. J.; Yao, Y. Design Principles for High Temperature Superconductors with Hydrogen-Based Alloy Backbone at Moderate Pressure. *Phys. Rev. Lett.* **2021**, *128*, 047001.
- (87) Edwards, B.; Ashcroft, N. W.; Lenosky, T. Layering Transitions and the Structure of Dense Hydrogen. *Europhys. Lett.* **1996**, *34*, 519.
- (88) Johnson, K. A.; Ashcroft, N. W. Structure and Bandgap Closure in Dense Hydrogen. *Nature* **2000**, *403*, 632–635.
- (89) Pickard, C. J.; Martinez-Canales, M.; Needs, R. J. Erratum: Density Functional Theory Study of Phase IV of Solid Hydrogen [Phys. Rev. B 85, 214114 (2012)]. *Phys. Rev. B* **2012**, *86*, 059902.
- (90) Cudazzo, P.; Profeta, G.; Sanna, A.; Floris, A.; Continenza, A.; Massidda, S.; Gross, E. K. U. Ab Initio Description of High-Temperature Superconductivity in Dense Molecular Hydrogen. *Phys. Rev. Lett.* **2008**, *100*, 257001.
- (91) Schackert, M.; Märkl, T.; Jandke, J.; Hölzer, M.; Ostanin, S.; Gross, E. K. U.; Ernst, A.; Wulfhekel, W. Local Measurement of the Eliashberg Function of Pb Islands: Enhancement of Electron-Phonon Coupling by Quantum Well States. *Phys. Rev. Lett.* **2015**, *114*, 047002.

- (92) Dangić, D.; Monacelli, L.; Bianco, R.; Mauri, F.; Errea, I. Large Impact of Phonon Lineshapes on the Superconductivity of Solid Hydrogen. *Commun. Phys.* **2024**, *7*, 150.
- (93) Mishra, A. K.; Muramatsu, T.; Liu, H.; Geballe, Z. M.; Somayazulu, M.; Ahart, M.; Baldini, M.; Meng, Y.; Zurek, E.; Hemley, R. J. New Calcium Hydrides with Mixed Atomic and Molecular Hydrogen. *J. Phys. Chem. C* **2018**, *122*, 19370–19378.
- (94) Bi, T.; Zurek, E. Electronic Structure and Superconductivity of Compressed Metal Tetrahydrides. *Chem. Eur. J.* **2021**, *27*, 14848–14870.
- (95) Yan, Y.; Bi, T.; Geng, N.; Wang, X.; Zurek, E. A Metastable CaSH₃ Phase Composed of HS Honeycomb Sheets That is Superconducting Under Pressure. *J. Phys. Chem. Lett.* **2020**, *11*, 9629–9636.
- (96) Deringer, V. L.; Tchougréeff, A. L.; Dronskowski, R. Crystal Orbital Hamilton Population (COHP) Analysis as Projected From Plane-Wave Basis Sets. *J. Phys. Chem. A* **2011**, *115*, 5461–5466.
- (97) Wang, X.; Bi, T.; Hilleke, K. P.; Lamichhane, A.; Hemley, R. J.; Zurek, E. Dilute Carbon in H₃S Under Pressure. *npj Comput. Mater.* **2022**, *8*, 87 (1–9).

Table of Contents Graphic

Superconducting Critical Temperature of Hydrides (T_c)



Supplemental Materials:
**A chemical bonding based descriptor for predicting the impact of
quantum nuclear and anharmonic effects on hydrogen-based
superconductors**

Projector Augmented Wave (PAW) Potentials

Table 1: The table reports the file name and valence electronic configurations for the PAW potentials used in the VASP calculations.

Element	File Name	Valence Configuration
H	PAW_PBE H	$1s^1$
B	PAW_PBE B	$2s^2 2p^1$
Al	PAW_PBE Al	$3s^2 3p^1$
S	PAW_PBE S	$3s^2 3p^4$
Sc	PAW_PBE Sc	$3d^2 4s^1$
Y	PAW_PBE Y_sv	$4s^2 5s^2 4p^6 4d^2$
Pd	PAW_PBE Pd	$4d^9 5s^1$
Pt	PAW_PBE Pt	$5d^9 6s^1$
La	PAW_PBE La	$5s^2 6s^2 5p^6 5d^1$

Phonons and Eliashberg Function of ScH_6 - $Cmcm$

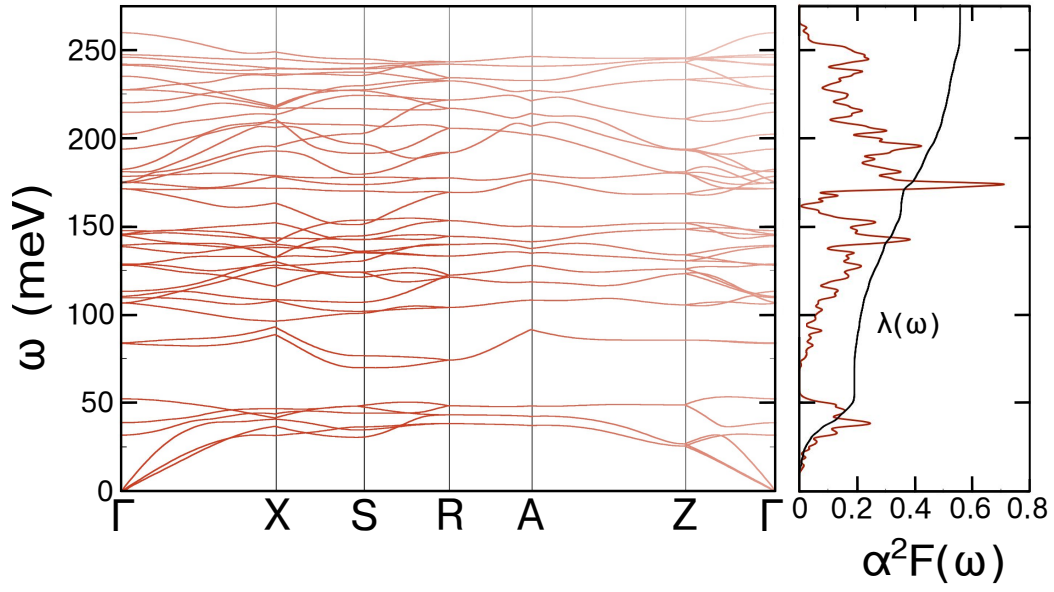


Figure S1: The classic phonon spectra for the ScH_6 - $Cmcm$ phase at 100 GPa (left), and the variation of the Eliashberg spectral function, $\alpha^2F(\omega)$, along with the integral of the electron phonon coupling parameter, $\lambda(\omega)$ (right), with the frequency.

Structural Parameters

Superconductivity

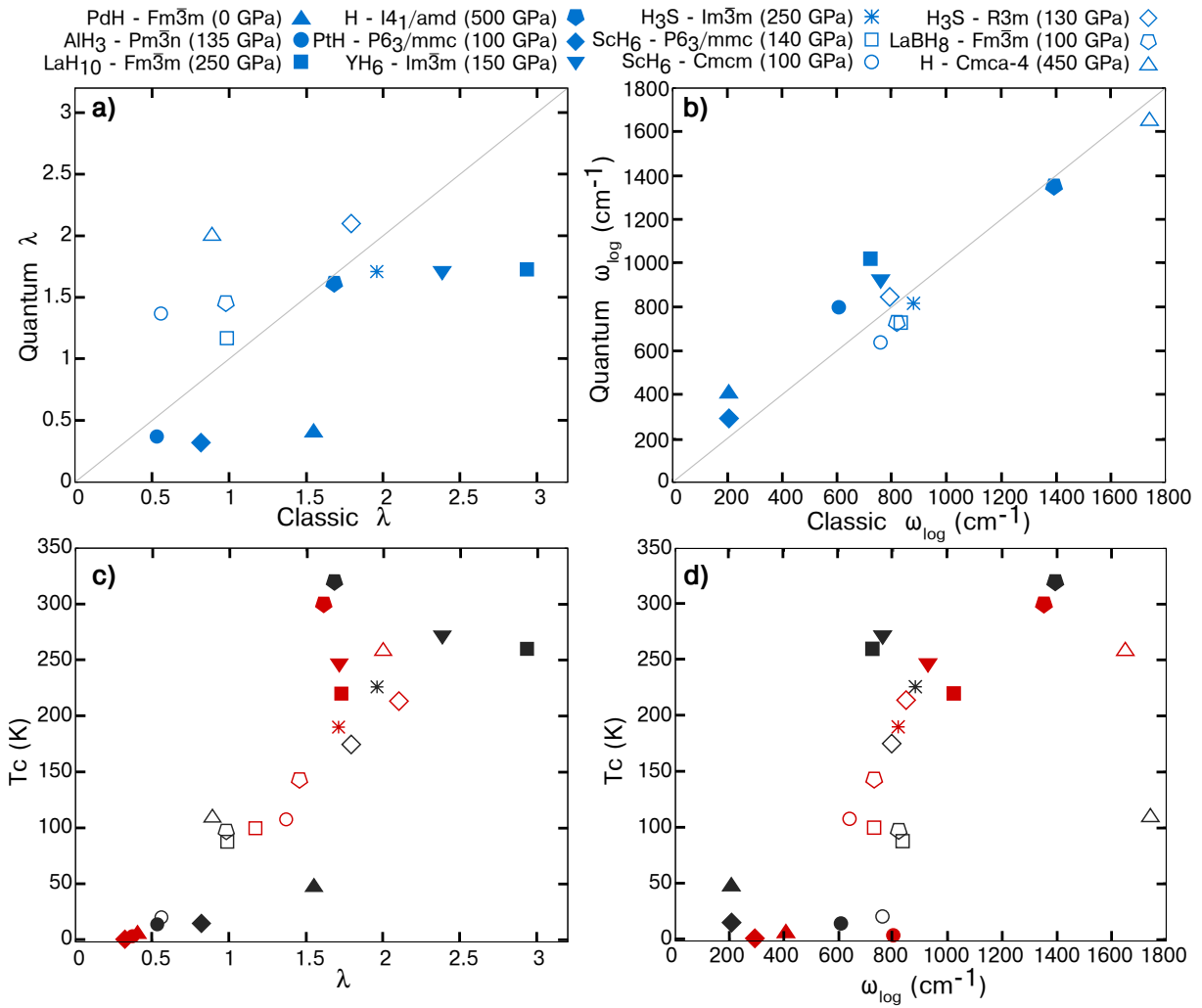


Figure S2: A comparison of (a) the electron phonon coupling parameter, λ , and (b) the logarithmic average phonon frequency, ω_{log} , between the classical and quantum structures. The line drawn in (a) and (b) corresponds to $y = x$. (c) The classic (black) and quantum (red) values of T_c as a function of λ . (d) The classic (black) and quantum (red) T_c as a function of ω_{log} .

Bonding Analysis

Table 2: The cell parameters and atomic positions for the considered compounds obtained when the nuclei were treated as classic particles.

Structure	Parameters	Atom	Wyckoff Site	Coordinate
PdH - $Fm\bar{3}m$ (1 atm)	$a = 4.132 \text{ \AA}$	Pd	4a	0.00 0.00 0.00
		H	4b	0.50 0.50 0.50
AlH ₃ - $Pm\bar{3}n$ (135 GPa)	$a = 3.003 \text{ \AA}$	Al	2a	0.00 0.00 0.00
		H	6c	0.50 0.25 0.00
LaH ₁₀ - $Fm\bar{3}m$ (250 GPa)	$a = 3.424 \text{ \AA}$	La	4b	0.50 0.50 0.50
		H	8c	0.25 0.25 0.25
		H	32f	0.10 0.10 0.10
H - $I4_1/amd$ (500 GPa)	$a = 1.120 \text{ \AA}$ $c = 3.110 \text{ \AA}$	H	4b	0.50 0.50 0.00
PtH - $P6_3/mmmc$ (100 GPa)	$a = 2.710 \text{ \AA}$ $c = 4.576 \text{ \AA}$ $\gamma = 120^\circ$	Pt	2d	0.33 0.67 0.75
		H	2a	0.00 0.00 0.00
YH ₆ - $Im\bar{3}m$ (150 GPa)	$a = 4.103 \text{ \AA}$	Y	2a	0.00 0.00 0.00
		H	12d	0.25 0.00 0.50
H ₃ S - $Im\bar{3}m$ (250 GPa)	$a = 3.007 \text{ \AA}$	S	2a	0.00 0.00 0.00
		H	6b	0.50 0.50 0.00
ScH ₆ - $P6_3/mmc$ (140 GPa)	$a = 3.406 \text{ \AA}$ $c = 4.255 \text{ \AA}$ $\gamma = 120^\circ$	Sc	2d	0.67 0.33 0.25
		H	12k	0.67 0.83 0.13
ScH ₆ - $Cmcm$ (100 GPa)	$a = 3.434 \text{ \AA}$ $b = 6.215 \text{ \AA}$ $c = 4.433 \text{ \AA}$	Sc	4c	0.00 0.33 0.75
		H	16h	0.75 0.43 0.36
		H	8f	0.83 0.66 0.89
H ₃ S - $R\bar{3}m$ (130 GPa)	$a = 3.116 \text{ \AA}$	S	3a	0.00 0.00 0.00
		H	9b	0.53 0.01 0.01
LaBH ₈ - $Fm\bar{3}m$ (200 GPa)	$a = 5.577 \text{ \AA}$	La	4b	0.50 0.50 0.50
		B	4a	0.00 0.00 0.00
		H	32f	0.15 0.15 0.15
H - $Cmca-4$ (450 GPa)	$a = 1.534 \text{ \AA}$ $b = 2.674 \text{ \AA}$ $c = 2.360 \text{ \AA}$	H	8f	0.00 0.37 0.43

Table 3: The electron phonon coupling (λ), logarithmic average phonon frequency (ω_{\log}), and superconducting critical temperature (T_c), for the classical and quantum structures divided into Type I (top) and Type II (bottom) families.

Structure	Classic			Quantum		
	λ	ω_{\log} (cm^{-1})	T_c (K)	λ	ω_{\log} (cm^{-1})	T_c (K)
PdH - $Fm\bar{3}m$ (1 atm)	1.55	205	47	0.40	405	5
AlH ₃ - $Pm\bar{3}n$ (135 GPa)	0.53	607	13.7	0.37	799	3.08
LaH ₁₀ - $Fm\bar{3}m$ (250 GPa)	2.93	722	260	1.72	1021	220
H - $I4_1/amd$ (500 GPa)	1.68	1393	320	1.61	1351	300
PtH - $P6_3/mmc$ (100 GPa)	0.82	205	14.5	0.32	291	0.378
YH ₆ - $Im\bar{3}m$ (150 GPa)	2.38	760	272	1.71	926	247
H ₃ S - $Im\bar{3}m$ (250 GPa)	1.96	879	226	1.71	817	190
ScH ₆ - $P6_3/mmc$ (140 GPa)	0.99	833	87.5	1.16	728	99.6
ScH ₆ - $Cmcm$ (100 GPa)	0.56	759	20	1.36	639	108
H ₃ S - $R\bar{3}m$ (130 GPa)	1.79	793	175	2.10	846	214
LaBH ₈ - $Fm\bar{3}m$ (100 GPa)	0.98	819	97	1.46	729	143
H - $Cmca-4$ (450 GPa)	0.89	1742	109	2.00	1650	258

Table 4: Distances and integrated crystal orbital bond indices (iCOBIs) for the listed atom pairs in the Type I compounds for which iCOBI ≥ 0.05 . The results were the same for the classical and quantum lattice for all of the compounds, except for LaH₁₀ where the two sets of values, respectively, are separated by a forward slash.

Structure	Atom Pair	Distance (Å)	iCOBI
PdH - $Fm\bar{3}m$	Pd-Pd	2.922	0.135
	Pd-H	2.066	0.138
AlH ₃ - $Pm\bar{3}n$	Al-H	1.678	0.161
LaH ₁₀ - $Fm\bar{3}m$	La - H	2.096 / 2.096	0.122 / 0.091
	La - H	2.053 / 2.015	0.115 / 0.145
	H - H	0.972 / 1.087	0.120 / 0.106
	H - H	1.254 / 1.165	0.055 / 0.072
H - $I4_1/amd$	H - H	0.985	0.144
PtH - $P6_3/mmc$	Pt - H	1.938	0.064
YH ₆ - $Im\bar{3}m$	Y - H	2.017	0.124
	H - H	1.275	0.053
H ₃ S - $Im\bar{3}m$	H - S	1.534	0.347

Table 5: The distances and integrated crystal orbital bond indices (iCOBIs) for the listed atom pairs in the Type II compounds calculated for both the classic and quantum lattices for which iCOBI ≥ 0.05 .

Structure	Atom Pair	Classic		Quantum	
		Distance (Å)	ICOBI	Distance (Å)	ICOBI
ScH ₆ - $P6_3/mmc$	H-H	1.020	0.240	1.068	0.220
	Sc-H	1.777	0.178	1.783	0.178
	Sc-H	1.896	0.137	1.884	0.141
	Sc-Sc	2.897	0.091	2.910	0.086
ScH ₆ - $Cmcm$	H-H	0.950	0.330	1.083	0.233
	H-H	1.275	0.117	1.083	0.233
	Sc-H	1.826(5)	0.169	1.833	0.174
	Sc-H	1.826(8)	0.195	1.833	0.174
	Sc-H	1.847	0.203	1.942	0.138
	Sc-H	2.032	0.102	1.942	0.138
	Sc-Sc	2.935	0.092	2.986	0.084
H ₃ S - $R3m$	H-S	1.456	0.463	1.559	0.347
	H-S	1.661	0.231	1.559	0.347
LaBH ₈ - $Fm\bar{3}m$	B-H	1.409	0.281	1.454	0.291
	B-La	2.788	0.164	2.788	0.150
	La-H	2.285	0.094	2.281	0.097
H - $Cmca-4$	H-H	0.782	0.424	0.832	0.358
	H-H	1.034	0.109	1.071	0.091
	H-H	1.158	0.051	1.079	0.086

Table 6: The symmetry inequivalent atoms and their Wyckoff positions in the Type I and Type II structures along with the corresponding symmetry index computed with the iCOHP instead of the iCOBI, $V(\text{iCOHP})_x = \frac{1}{B_x} \sum_{\alpha=1}^{B_x} \text{iCOHP}(x, \alpha) \mathbf{i}_{x\alpha}$ and $S(\text{iCOHP})_x = |V(\text{iCOHP})_x|$ (see main text), treating the nuclei as classical, $S(\text{iCOHP})_a^c$, and quantum, $S(\text{iCOHP})_a^q$, objects. The iCOHP based results are not able to distinguish between Type I and Type II structures as the value of $S(\text{iCOHP})_a^c$ for the hydrogens at the 32f site in LaH_{10} is greater than the Type II H - $Cmca$ -4 structure. The Wyckoff parameters given in parenthesis for ScH_6 - $Cmcm$ correspond to the symmetry site and multiplicity of the equivalent atoms in the higher symmetry ScH_6 - $P6_3/mmc$ phase. Additionally, the values of the iCOHP used in the analysis have been selected using a cutoff of 0.5 (eV/bond), so as to consider the same amount of interactions reported in the iCOBI analysis.

Structure	Atom	Wyckoff letter	$S(\text{iCOHP})_a^c$ (eV/bond)	$S(\text{iCOHP})_a^q$ (eV/bond)
Type I				
PdH - $Fm\bar{3}m$	Pd	4a	0	0
	H	4b	0	0
AlH_3 - $Pm\bar{3}n$	Al	2a	0	0
	H	6c	0	0
LaH_{10} - $Fm\bar{3}m$	La	4b	0.00	0
	H	8c	0.01	0.01
	H	32f	0.22	0.08
H - $I4_1/amd$	H	4b	0	0
PtH - $P6_3/mmc$	Pt	2d	0	0
	H	2a	0	0
YH_6 - $Im\bar{3}m$	Y	2a	0	0
	H	12d	0	0
H_3S - $Im\bar{3}m$	S	2a	0	0
	H	6b	0	0
Type II				
ScH_6 - $P6_3/mmc$	Sc	2d	0	0
	H	12k	0.52	0.48
ScH_6 - $Cmcm$	Sc	4c	0.00	0 (2d)
	H	16h	0.33	0.47 (12k)
	H	8f	0.77	0.47 (12k)
H_3S - $R3m$	S	3a	0.68	0
	H	9b	1.03	0
LaBH_8 - $Fm\bar{3}m$	La	4b	0	0
	B	4a	0	0
	H	32f	0.70	0.73
H - $Cmca$ -4	H	8f	0.17	0.09

Table 7: The symmetry inequivalent atoms and their Wyckoff positions in the Type I and Type II structures along with the corresponding symmetry index computed with the magnitudes of the interatomic distances, $\mathbf{V}(\mathbf{d})_x = \frac{1}{B_x} \sum_{\alpha=1}^{B_x} \mathbf{d}(x, \alpha) \mathbf{i}_{x\alpha}$ and $S(\mathbf{d})_x = |\mathbf{V}(\mathbf{d})_x|$ (see main text), treating the nuclei as classical, $S(\mathbf{d})_a^c$, and quantum, $S(\mathbf{d})_a^q$, objects. Here $\mathbf{d}(x, \alpha)$ is the interatomic distance between atoms x and α . The distance based results are not able to distinguish between Type I and Type II structures as the value of $S(\mathbf{d})_a^c$ for the hydrogens at the 32f site in LaH_{10} is greater than the $S(\mathbf{d})_a^c$ for both atoms in the Type II $\text{H}_3\text{S} - R\bar{3}m$ structure. The Wyckoff parameters given in parenthesis for $\text{ScH}_6 - Cmc\bar{m}$ correspond to the symmetry site and multiplicity of the equivalent atoms in the higher symmetry $\text{ScH}_6 - P6_3/mmc$ phase. The interatomic distances considered in this analysis correspond to those considered for the iCOBI analysis.

Structure	atom	Wyckoff letter	$S(\mathbf{d})_a^c$ (Å)	$S(\mathbf{d})_a^q$ (Å)
Type 1				
$\text{PdH} - Fm\bar{3}m$	Pd	4a	0	0
	H	4b	0	0
$\text{AlH}_3 - Pm\bar{3}n$	Al	2a	0	0
	H	6c	0	0
$\text{LaH}_{10} - Fm\bar{3}m$	La	4b	0	0
	H	8c	0.00	0
	H	32f	0.18	0.03
$\text{H} - I4_1/amd$	H	4b	0	0
$\text{PtH} - P6_3/mmc$	Pt	2d	0	0
	H	2a	0	0
$\text{YH}_6 - Im\bar{3}m$	Y	2a	0	0
	H	12d	0	0
$\text{H}_3\text{S} - Im\bar{3}m$	S	2a	0	0
	H	6b	0	0
Type 2				
$\text{ScH}_6 - P6_3/mmc$	Sc	2d	0	0
	H	12k	0.29	0.32
$\text{ScH}_6 - Cmc\bar{m}$	Sc	4c	0.38	0 (2d)
	H	16h	0.41	0.32 (12k)
	H	8f	0.26	0.32 (12k)
$\text{H}_3\text{S} - R\bar{3}m$	S	3a	0.02	0
	H	9b	0.11	0
$\text{LaBH}_8 - Fm\bar{3}m$	La	4b	0	0
	B	4a	0	0
	H	32f	0.20	0.25
$\text{H} - Cmca-4$	H	8f	0.29	0.22